Heating Water with Wind or Hydro Power:

Direct Conversion of Mechanical Energy to Heat Using Eddy Currents

Undergraduate Honors Thesis

By

Peter Worley

Advisor: Dr. Vish Subramaniam

Department of Mechanical and Aerospace Engineering

The Ohio State University

Spring 2015

Abstract

On average in the United States, approximately 18% of total residential energy consumption is for heating water. Current methods for heating water, involving electrical resistive heaters and natural gas heaters, are inefficient and depend upon the burning of fossil fuels which release greenhouse gases. This proposal discusses a novel way to heat water, known as an eddy current water heater (ECWH), by directly converting the mechanical energy of a rotating disk (e.g. driven by a wind or water turbine), in a fixed magnetic field, into heat by using eddy currents. Electrical eddy currents are induced in any conductor moving in a magnetic field in accordance with Faraday's law. If these eddy currents are not extracted from the disk, the currents will dissipate as heat. The goal of this research is to gain a better understanding of the physical relationships in a laboratory scale model to enable practical eddy current water heating systems to be developed. The relationships between the disc's angular velocity, the permanent magnets field strength, and the resulting resistive torque are investigated using an eddy current dynamometer. Data were collected on these three variables in order to evaluate the accuracy of current theoretical models as well as to establish the relevant non-dimensional groupings to allow for scaling from a model to a prototype. A non-dimensional parameter of significance has been found, which can be used to scale the laboratory scale model to a prototype for residential use. Furthermore, it is shown that current theoretical models do not reliably predict power dissipation and resistive torque. Thus current theoretical models could be improved as they consider simpler disk to magnet geometries and lower speeds than may be required for a practical ECWH design. The results presented here underscore the need for further study of how eddy currents form and flow in a given ECWH design, specifically the skin effect and the paths of the eddy currents outside the magnet area.

Acknowledgements

I would like to thank my research advisor, Dr. Vish Subramaniam, for his guidance and mentorship throughout this entire research experience. I appreciate the time he took to meet with me every week as well as the time he graciously gave to me on evenings and weekends to allow me to put my best foot forward. I thank him for his patience too.

I would like to thank Joe West and Dan Langstaff for their technical assistance as well theoretical explanations. They helped in troubleshooting issues with eddy current dynamometer and were able to provide strong explanations to my copious amount of questions.

I would like to thank Derek Recker and Dr. Blaine Lilly from ME 2900 for graciously lending me the eddy current dynamometer.

I would like to thank the College of Engineering for its financial support through the generous Undergraduate Research Scholarship.

And very importantly, I would like to thank my friends and family for the consistent encouragement they gave me as I dedicated my time more and more to this research. I am grateful for their positive influences.

Table of Contents

List of Figures

List of Tables

List of Equations

List of Variables

j – Volume current density (A/m^3)

B – Magnetic field strength (Tesla)

R – Distance from center of disk to center of magnet pole (m)

ρ – Resistivity of disk (Ohm-m)

σ – Conductivity of disk (Siemens/m)

$\dot{\boldsymbol{P}}_{\boldsymbol{d}}$ – Power dissipated volume density (W/m^3)

P_d – Power dissipated (W)

D – Diameter of magnet (m)

t – Thickness of disk (m)

T – Resistive torque on disk (N-m)

$\boldsymbol{a}$ – Radius of rotating disk (m)

δ – Depth of eddy currents in conductor (m)

f – Frequency of the changing electromagnetic field (Hz)

μ – Permeability of conductor (H/m)

Chapter 1: Introduction

1.1 Current Technology for Heating Water for Residential Use in the United States

Increasing global demands require innovative solutions to daily energy consumption. Heating water accounts for 18% of U.S residential energy consumption [1], which translates to an annual bill of $400-$600 in 2013 [2]. Usually, residential water is periodically heated by burning natural gas in a multi-gallon hot water heater, which releases greenhouse gasses into the atmosphere. In comparison, electric resistive heaters can utilize carbon-free electricity generation from solar panels or wind turbines, however, conversion of precious electrical energy into heat (low availability in the thermodynamics sense) is not effective or efficient use of high quality (i.e. high availability) energy.

1.2 Heating Water using Eddy Currents

In this research, a novel method for heating water using electrical eddy currents is explored. Electrical eddy currents are closed paths of electrical current that are induced in a conductor moving in a magnetic field due to Faraday's law. This concept is related to the Faraday disk generator shown in Figs. 1-2, where electrical current can be drawn from a conducting disk spinning in a magnetic field due to a potential difference generated between the shaft and the rim of the disk.

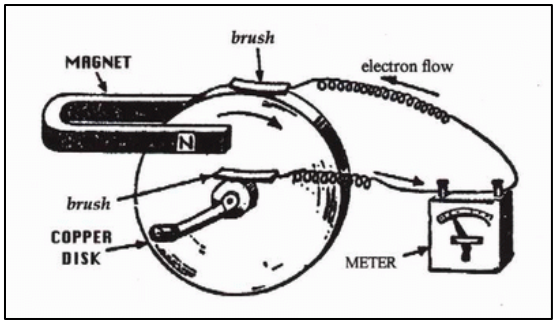

Figure 1: Diagram of Faraday Disk Generator [3]

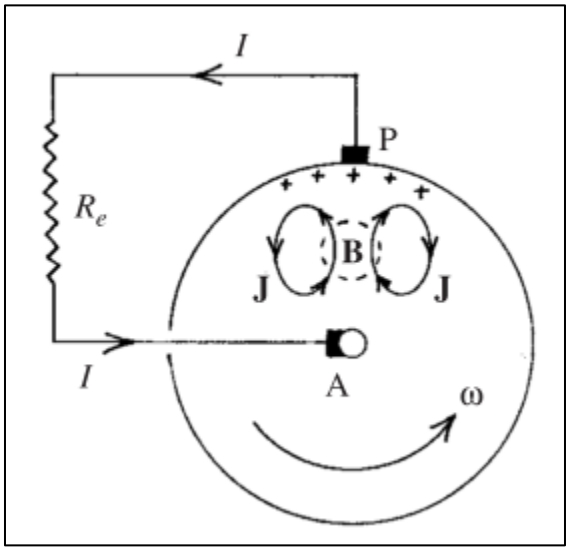

Figure 2: Schematic of potential difference and extracted current from eddy currents in Faraday Disk Generator [4]

In the proposed concept, if no electrical current is drawn from a device such as those shown in Figs. 1-2, then the electrical currents flow within the disk as eddy currents and are Ohmically converted to heat, which is shown in Fig. 3. It is this type of heating which is explored in this research. This method of heating water through contact with a metal disk heated by eddy currents is referred to here as eddy current water heating (ECWH).

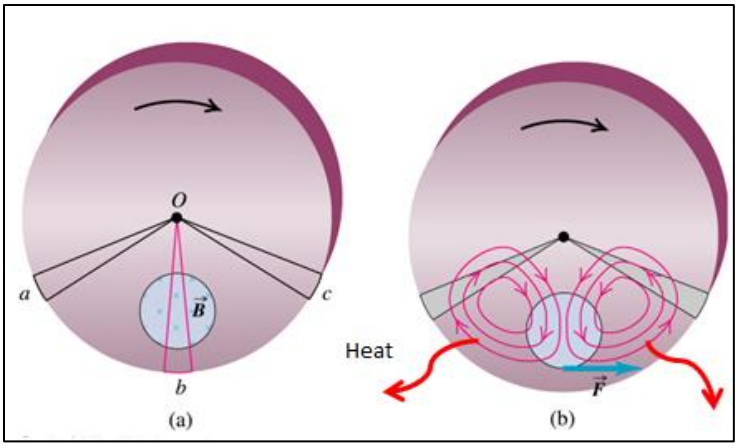

Figure 3: Schematic of heating disk of ECWH where eddy currents are not extracted [5]

ECWH could be used in a traditional multi-gallon storage tank design as shown in Fig. 4 as well as a design meant only to heat flowing water. It is presumed that the power source for rotation of the metal disk in the magnetic field is derived from a wind turbine or hydro turbine, so that it does not emit greenhouse gases by burning fossil fuels directly to heat the water or by requiring electrical power that is generated by burning fossil fuels.

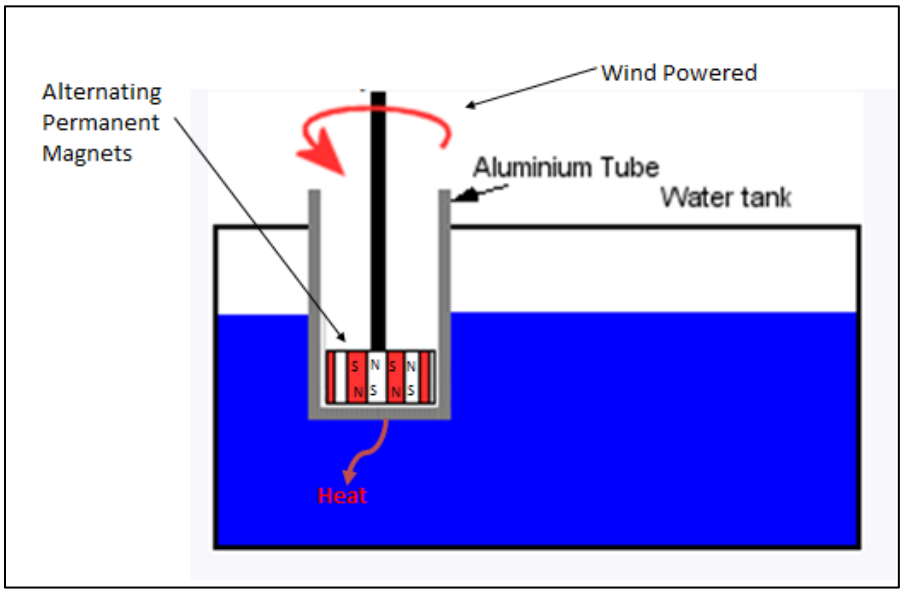

Figure 4: Example design of a storage tank eddy current water heater [6]

ECWH is promising because it *directly* transfers mechanical energy to heat via eddy currents. Other methods that use electricity to create heat must first convert mechanical energy or energy of another form into electricity which may then be converted into heat by Joule heating, or require combustion of a fossil fuel. The intermediate steps required to create electricity each have associated energy losses. A diagram juxtaposing these conversion paths is shown in Fig. 5.

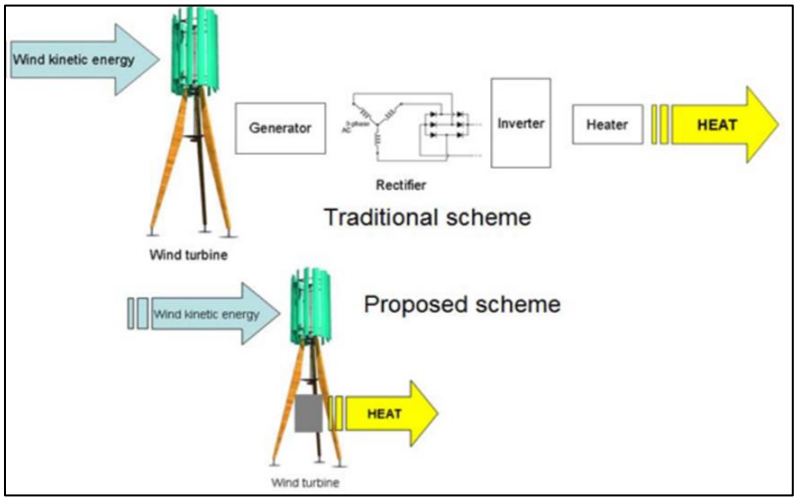

Figure 5: Schematic of energy conversion schemes from renewable sources [7]

1.3 Background

Eddy currents can produce significant heating as it is observed in eddy current dynamometers widely used in industry as well as eddy current brake systems commonly found in systems such as roller coasters and high speed trains. Additionally, it has already been shown experimentally that a metal plate can raise 40 ^{o}F in less than 10 minutes when a disk with an array of 16 magnets spins at 400 rpm at a separation gap of three mm [8]. As a point of comparison, a state-of-the-art (standard) water heater intakes water at 58 ^{o}F and raises it to 135 ^{o}F [2]. ECWH is especially intriguing now because of the low cost of rare earth magnets in comparison to prices 20 years ago [9].

The vast majority of published work considers the problem from a theoretical or computational perspective (e.g. Dirba, 2014 [7]; Fireteanu, 2008 [10]; Nebi, 2010 [11]; and Tudorache, 2009 [12]). Moreover, the only experimental measurement that exists (Liu, 2011 [8]) uses an electric motor to turn a metal disk to specific rotational speeds so as to monitor temperature rise versus rpm. These results were reported in a conference proceeding and are incomplete in terms of providing information necessary for scale-up of the concept to a prototype. Moreover, in reality, there are counteracting forces arising from the interaction of the magnetic field with the induced eddy currents, applying a resistive torque to the shaft. This has not been explored in detail in the literature.

1.4 Theoretical Models for Resistive Torque

The physics of the counteracting force, i.e the resistive torque, when a metal disk rotates in the presence of a magnetic field applied in the same direction as its axis, is similar to that in eddy current braking used for roller coasters, trains, and industrial machines. However, it is important to recognize the distinction in application for ECWH versus braking. Literature on eddy current braking in addition to ECWH was reviewed to determine if models exist that could predict the amount of resistive torque created by eddy currents on a spinning metal disk. Gosline et. al, present a simple approach for calculating torque, making several simplifying assumptions in order to keep the physics at a basic level [13]. This approach is referred to here as the Simple model. First, spinning the disk under a pole of a magnet establishes a changing magnetic field, which induces an electric field (i.e a motional emf) in the disk under the area of the magnet in accordance with Faraday's Law. The induced electric field then generates an eddy current. The induced current density is given by [13],

$$j = \frac{E}{\rho} = \frac{Bv}{\rho} = \frac{BR\omega}{\rho} = \sigma BR\omega \quad (1)$$

where, j is the current density (A/m^2), E is the electric field (V/m), ρ is the resistivity of the disk (Ohm-m), B is the magnetic field strength (Tesla), v is the velocity of the magnet (m/s), R is the distance from the center of the disk to the center of the magnet pole (m), ω is the angular velocity of the disk (rad/s), and σ is the conductivity of the disk (Siemens/m).

The power dissipated per unit volume by the eddy currents through Ohmic heating is given by,

$$P_d = j^2\rho = \frac{j^2}{\sigma} = \frac{(\sigma BR\omega)^2}{\sigma} \quad (2)$$

where, P_d is the power dissipated per unit volume (W/m^3).

One of the major assumptions of the Simple model is that the induced current flows only under the immediate area of the magnet pole. Thus, the electrical resistance imposed on the induced current is the volumetric resistivity of the cylinder portion of the disk under the magnet pole modeled in the same fashion as the resistance of a current carrying wire. A schematic depicting this assumed situation is shown schematically in Fig. 6.

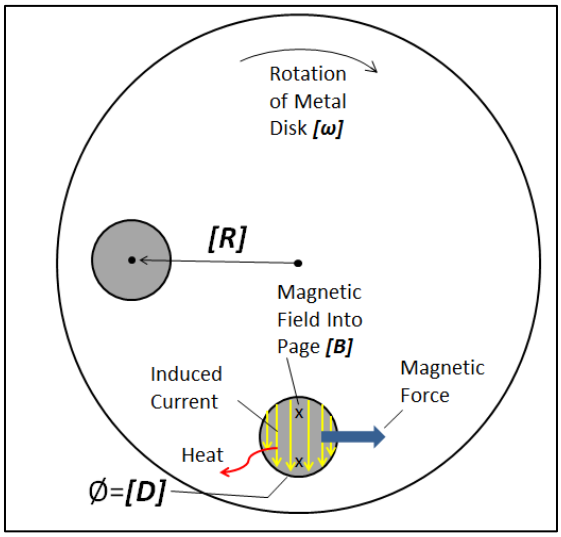

Figure 6: Schematic of the location of the induced currents in the Simple model

Therefore, the total power dissipated (i.e heat generated) is determined by integrating over the cylindrical volume:

$$\boldsymbol{P_d = \frac{\pi}{4}\sigma D^2 t B^2 R^2 \omega^2} \quad \textbf{(3)}$$

where, P_d is the power dissipated by the eddy currents, D is the diameter of the magnets (m), and t is the thickness of the disk (m).

Lastly, the torque can be determined from the power dissipation equation as the power dissipated divided by angular velocity, assuming no losses in the transmission of the torque

$$\boldsymbol{T = \frac{P_d}{\omega} = \frac{\frac{\pi}{4}\sigma D^2 t B^2 R^2 \omega^2}{\omega} = \frac{\pi}{4}\sigma D^2 t B^2 R^2 \omega}$$

where, T is the resistive torque exerted on the rotating disk (N-m).

Thus the resistive torque predicted by the Simple Model is,

$$\boldsymbol{T = \frac{\pi}{4}\sigma D^2 t B^2 R^2 \omega} \quad \textbf{(4)}$$

The torque is a result of the magnetic force exerted on the current passing under the area of the magnet, in accordance to Lorentz's Law. This can be seen in Fig. 6 shown earlier.

A deeper investigation into the literature of eddy current braking uncovered that there were three relevant articles on the subject, each with their own formula: Smythe, 1942 [14]; Schieber, 1974 [15]; and Wouterse 1991 [16], each built upon the work of the previous. Schieber's formula is the most appropriate for this study as it is based on using permanent magnets and accounts for the geometry of the circular paths of the eddy currents in the disk. Schieber attempts to provide a general solution to braking torque while Smythe concentrates on a specific geometry. Wouterse's focus is on electromagnets and the demagnetizing effects of the eddy currents on them, which is not relevant to an eddy current water heater that uses permanent

magnets. Schieber's formula for the resistive torque exerted by eddy currents on a rotating disk by one magnet pole is given as:

$$\boldsymbol{Torque = \frac{\pi}{8} D^2 t \sigma B^2 R^2 \omega \left[1 - \left(\frac{\frac{D}{2}}{a}\right)^2 \Big/ \left(1 - \left(\frac{R}{a}\right)^2\right)^2\right]} \quad \textbf{(5)}$$

where, a is the diameter of the rotating disk (m). As discussed earlier with the Simple model, since power dissipation is the product of resistive torque and angular velocity, the power dissipated by eddy currents according to Schieber's model is,

$$\boldsymbol{P_d = \frac{\pi}{8} D^2 t \sigma B^2 R^2 \omega^2 \left[1 - \left(\frac{\frac{D}{2}}{a}\right)^2 \Big/ \left(1 - \left(\frac{R}{a}\right)^2\right)^2\right]} \quad \textbf{(6)}$$

Schieber's model is derived in a similar manner to the Simple model (Equation 3) using Faraday's Law of Induction. One key difference between the two is that Schieber's model does not confine the current to the cylindrical volume under the magnet. Instead, Schieber's model more accurately considers the current to travel throughout the disk in the form of eddy currents, circling about the edges of the magnet area – a schematic of which is shown in Fig. 7.

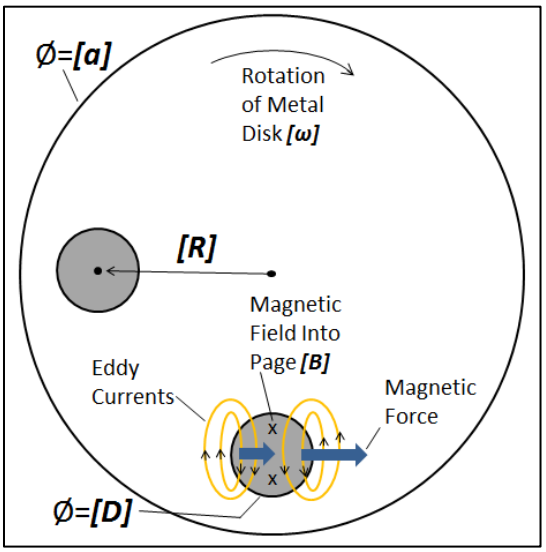

Figure 7: Schematic of eddy current paths in heating disk and identified geometry parameters for Schieber's model

A more detailed diagram from Schieber depicting the expected paths of the eddy currents in a rotating disk in the presence of two magnets, is shown in Fig. 8 [15].

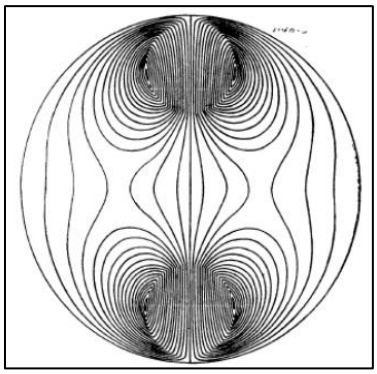

Figure 8: Diagram of the eddy current paths in a rotating disk in the presence of two magnets [15]

Schieber's model (Equation 6) is nearly identical as that of the Simple model but for a geometric coefficient which accounts for the eddy current paths. The geometric coefficient is always less than one, so that Schieber's model will always predict a smaller power dissipation than the Simple model. Schieber's model predicts less torque as well because with the eddy currents traveling outside the area of the magnet, the induced current faces more resistance, which means less current traveling under the area of the magnet, and thus less magnetic force. Another key difference between the two models is that Schieber assumes the plate is infinitesimally small and has an infinitely large conductivity. This is not the case for an ECWH.

It is not clear whether either the Simple model or the Schieber model can accurately describe the power dissipation and torque occurring in an ECWH because its operation is fundamentally different than a brake system. The sole function of an eddy current brake is to stop motion, while an ECWH functions to generate heat and must therefore continuously rotate. The endless rotating or large number of magnets of an ECWH could introduce different dynamics. Thus, these models need to be experimentally validated for the case of an ECWH.

Chapter 2: Objectives

2.1 Experimental Objectives

The goal of this work is to experimentally study ECWH with a focus on a key practical factor: torque exerted on the spinning, heating disk. Existing work on ECWH has neglected to examine this factor, and it is unclear whether eddy current brake torque formulas can translate to ECWH analysis and design. Resistive torque, a critical design parameter, must be better understood in order to make good ECWH designs. Once design parameters are better understood it can then be determined if eddy current water heating is feasible and whether it is a viable alternative to current methods used to heat water. Before discussions of economic feasibility occur, the underlying physics need to be better understood.

In this work, ECWH is explored in-depth experimentally and in a methodical manner. Since wind and hydro sources are difficult to replicate in the laboratory, a physical benchtop model is used to investigate resistive torque and the variables essential to torque. The variables essential to torque that need to be investigated are heating disk geometry, angular velocity, magnetic field strength, and their interrelation with the torque. The benchtop model is a modified eddy current dynamometer with ten permanent magnets as shown in Fig. 9. In addition, dimensional analysis is used to relate measurements on the model to infer corresponding relationships of critical parameters for a prototype.

Chapter 3: Experimental Apparatus and Procedure

3.1 Eddy Current Dynamometer

The benchtop model used to replicate ECWH was an eddy current dynamometer, powered by an electric motor. The motor is AC, single phase, and rated at 1/3 hp at 1750 rpm. Its speed cannot be controlled. It is designed to run at 1750 rpm, however lower speeds are attainable if excessive load is put on the motor. The eddy current dynamometer not only replicates an ECWH but also provides the capability to perform measurements on the essential variables: angular velocity and torque. Fig. 9 shows the experimental setup.

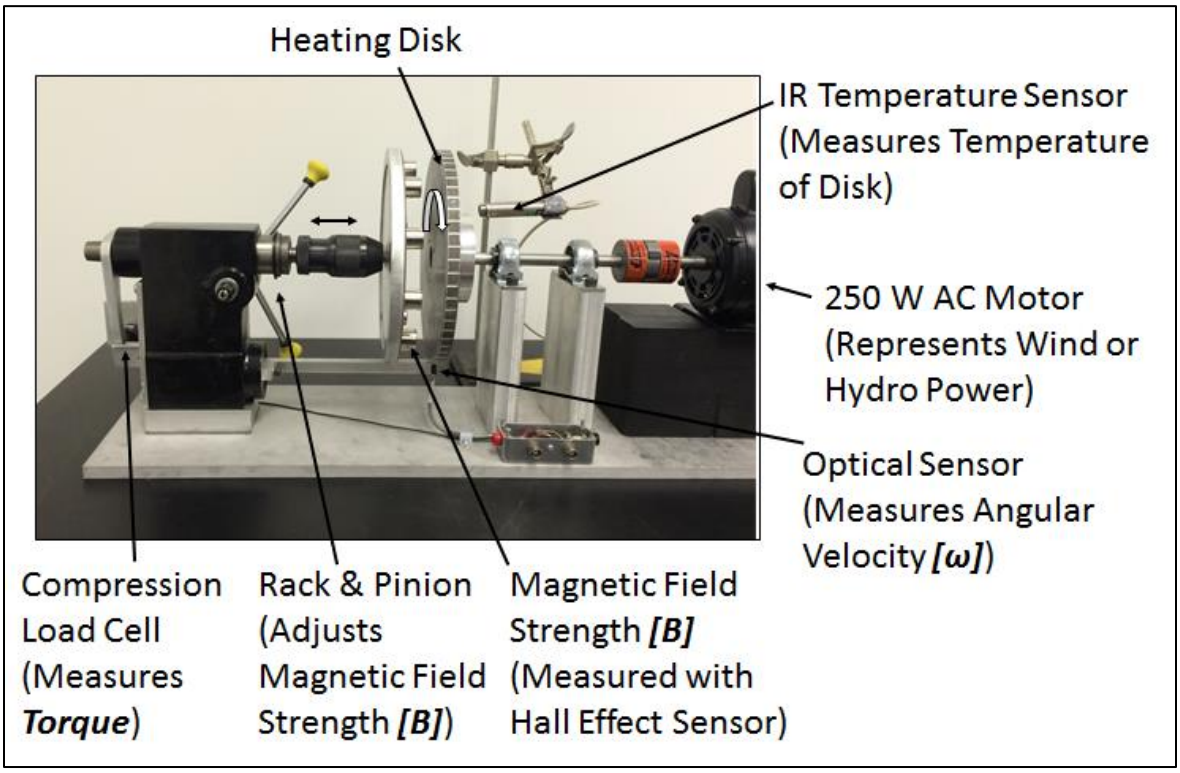

Figure 9: Experimental setup of eddy current dynamometer used as benchtop model

Conditions with different magnetic field strengths, rotational velocities, and torque were explored. Rotational velocity is measured using an optical sensor (OPB 742, OPTEK) and

torque is monitored using a compression load cell (0.5 V – 4.5 V, 50 lbf operating force). In addition, the temperature of the disk is measured approximately three inches radially outward from the center of the disk using an infrared pyrometer (OS152-MT IR Temperature Sensor, Omega) in order to track the temperature rise. All of the measurements devices are connected to a National Instruments NI-USB 6211 data acquisition device (NI-Daq). Matlab is used to control the NI-Daq, record the measurements, and analyze the data.

3.2 Experimental Procedure

The rotational velocity, torque, and magnetic field strength are all changed by adjusting the distance between the magnets and the rotating disk. The rack and pinion system shown in Fig. 9 – an adapted drill press spindle - adjusts the distance of the magnets from the spinning disk. By bringing the magnets closer the magnetic field strength experienced by the rotating aluminum 6061 disk increases, which then slows the rotational velocity in accordance with the motor's torque-speed curve. Angular velocity, torque, magnetic field strength, and disk temperature are recorded at eight different magnet distances (i.e. magnetic field strengths). Five trials of 60 seconds each were performed at each distance. Furthermore, one 10 minute trial was performed at each distance in order to better capture temperature rise of the disk.

3.3 Measurement of Magnetic Field Strength

The first step in the experimental procedure is setting the distance between the magnets and the disk using a shim, as shown in Fig. 10.

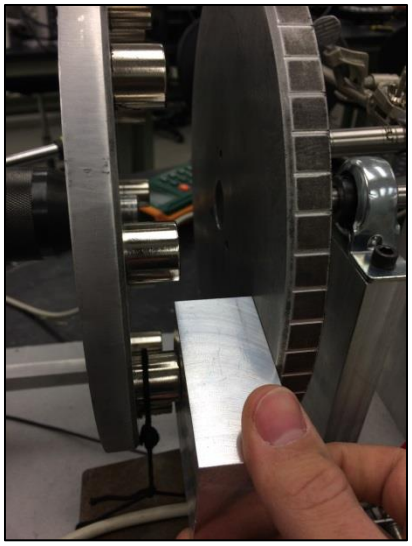

Figure 10: Example of using a shim to set the distance between the magnets and the rotating disk

Eight shims of known thickness are used to set eight discrete, different magnetic field strengths. Dial calipers were used to determine the thickness of the shims. A PASCO CI-6520A Hall effect sensor was used to determine the magnetic field strength at the different distances, as shown in Fig. 11.

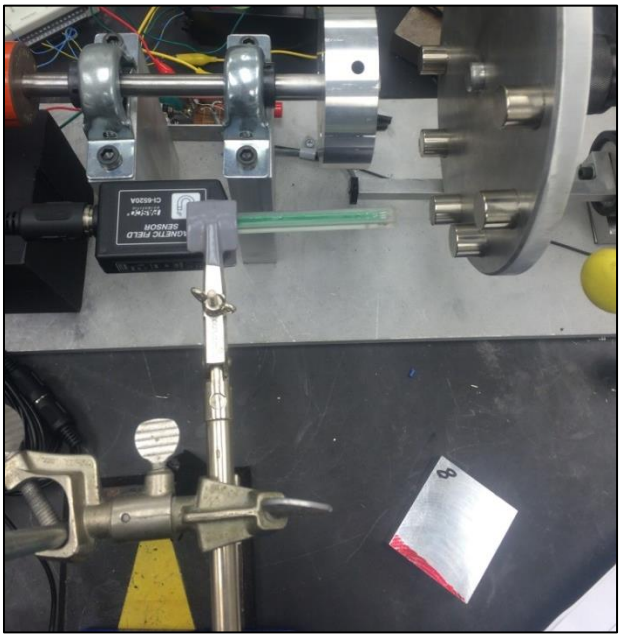

Figure 11: Use of hall effect sensor to measure magnetic field strength at shim distances

Table 1 displays the magnetic field strength at various shim thicknesses. The magnets used in the dynamometer were class-four Neodymium permanent magnets. There were 10 magnets evenly spaced apart and alternating in polarity.

Table 1: Measurements of shim thickness

Shim Number	Thickness (in)	Total Magnetic Field Strength (T)
8	1.216	0.048
7	0.947	0.114
6	0.752	0.214
5	0.689	0.262
4	0.629	0.318
3	0.493	0.493
2	0.375	0.721
1	0.311	0.886

The Hall-effect sensor was confirmed to be reading accurate values because it registered 0.105 T at the surface of the magnets, which is typical for class-four Neodymium magnets of their size. After the distances of the magnets were set, the electric motor was turned on and measurements were taken.

3.4 Measurement of Angular Velocity

Angular velocity is measured using an optical sensor (OPB 742, OPTEK). Along the circumferential side of the rotating disk there are 60 evenly spaced silver segments with black segments alternating in between. This can be seen in Fig. 10. The optical sensor outputs a higher voltage (approximately 4 V) when it is under a black segment of the side of the rotating disk and outputs a lower voltage (approximately 0.1 V) when it is under a silver segment, an example of which can be seen in Fig. 12.

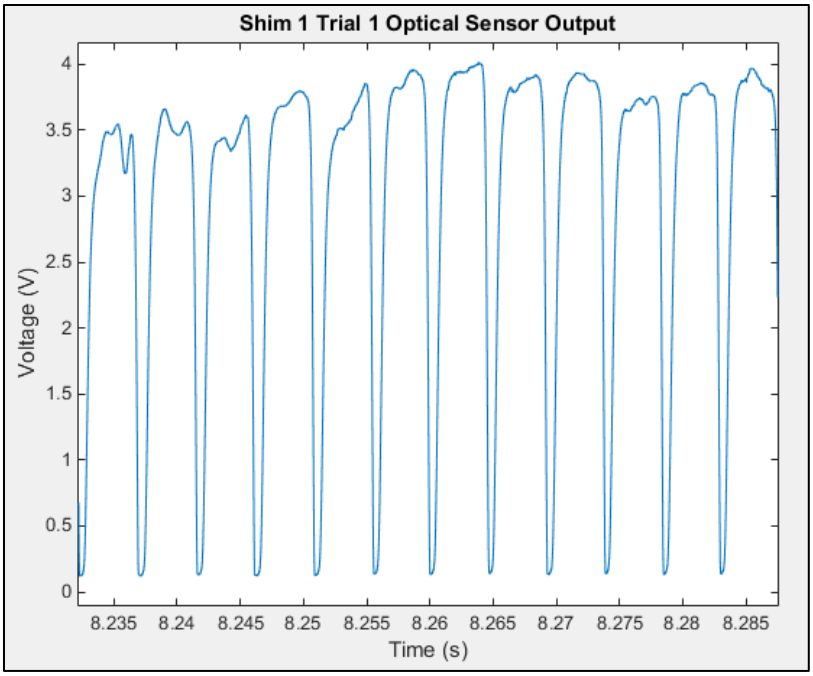

Figure 12: Example of high voltage, low voltage output of optical sensor

There are 60 evenly spaced silver segments on the side of the disk, thus the frequency of the optical sensor output in Hz corresponds exactly to the revolutions per minute of the rotating disk. The optical sensor was confirmed to be providing accurate measurements because when a small load was placed on the motor the optical sensor output frequency equaled 1750 Hz, which translated to 1750 rpm - the rated rpm of the motor.

3.5 Measurement of Torque

Torque was measured using a compression load cell (0.5 V – 4.5 V, 50 lbf operating force). As the heating disk rotates, it experiences a resistive torque through the magnetic force on the induced currents under the area of the magnet. An equal and opposite force is exerted back on the magnets which is transferred through the spindle through the moment arm and to the compression load cell. The load cell output is calibrated for torque by hanging known weights on the magnet disk at a known moment arm, as can be seen in Fig. 13.

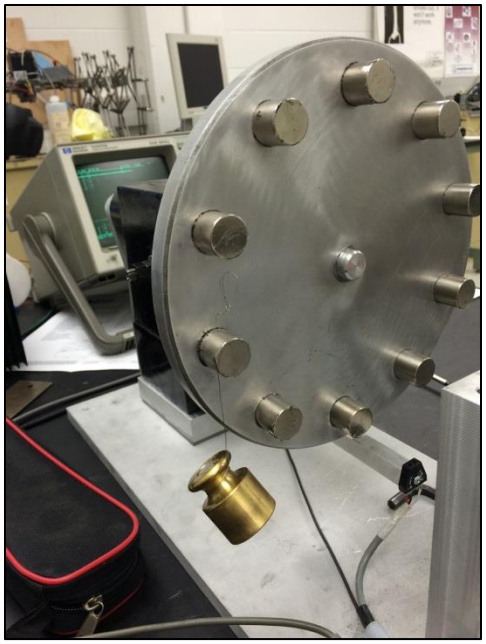

Figure 13: Calibration of load cell by hanging weights on magnet disk

A calibration curve (Appendix A, Table 6, Fig. 27) was constructed with three data points of torque vs load cell output. During preliminary testing the torque readings had extreme oscillations at high speeds as can be seen in Fig. 14.

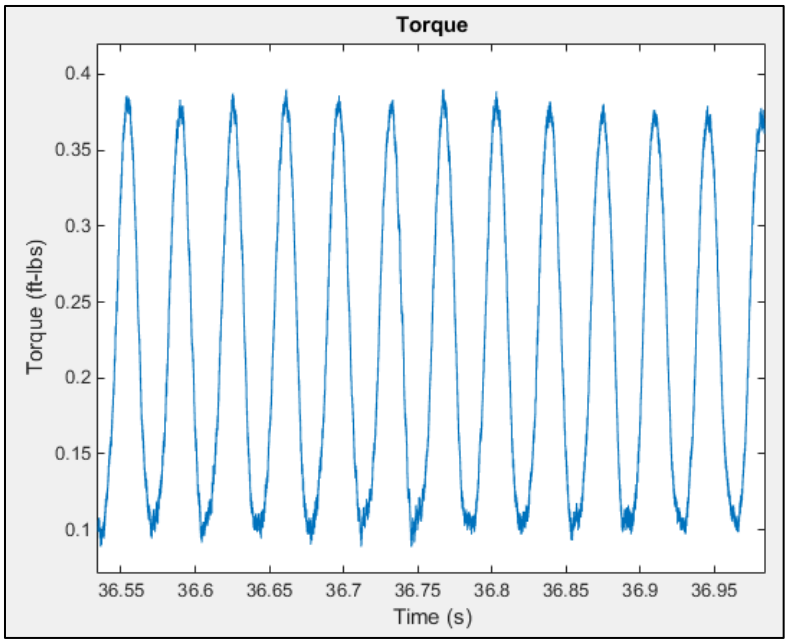

Figure 14: An example of extreme oscillations in torque readings during preliminary testing

It can be seen in Fig. 14 that the torque oscillations are periodic. The frequency of the torque oscillations is found to match the frequency of the motor at frequencies between 25 and 30 Hz corresponding to 1500 rpm and 1800 rpm, respectively. Fig. 15 shows a preliminary test where over 90 seconds the magnets were brought closer to the disk over intervals and subsequently slowed down the motor. The peak at 45 seconds is the point at which the motor speed rapidly dropped from approximately 1500 rpm down to 500 rpm due to the motor's torque-speed characteristics.

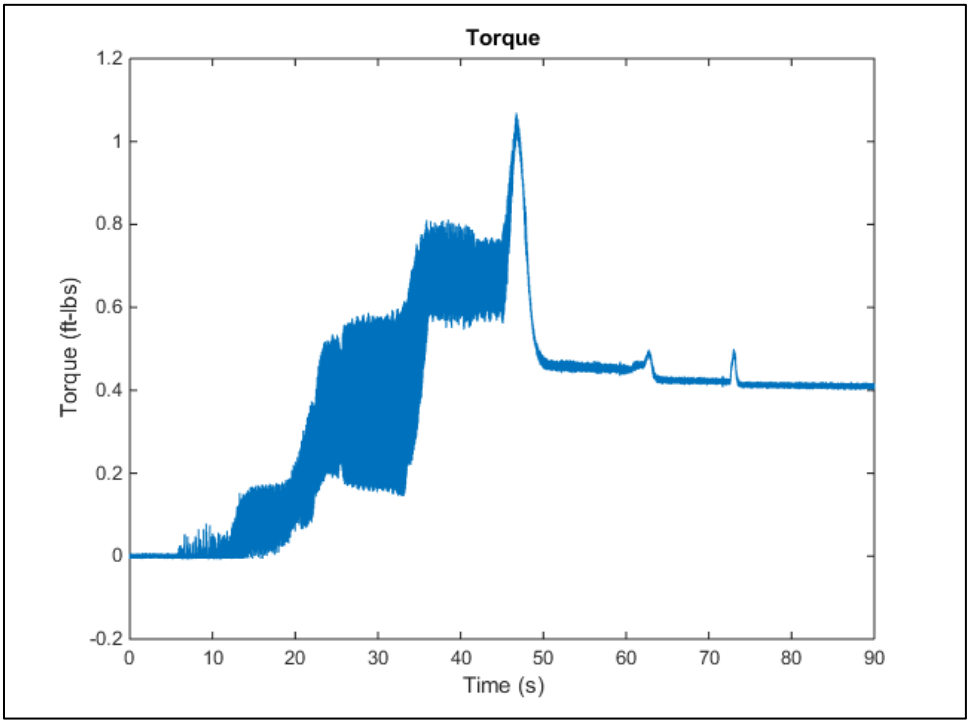

Figure 15: Preliminary test showing high torque oscillations at high speeds (25 to 45 second mark) and no oscillations at low speeds (after 45 seconds)

High torque oscillations occurred at around 25 seconds (1750 rpm, 29 Hz) and 40 (1500 rpm, 25 Hz). This raises concerns that the torque measurement system comprising of the magnet disk, spindle, moment arm, and load cell platform, act as a torsional spring with a resonant frequency in the range of 25 and 30 Hz, coincidentally directly in the range of the motor operating speed.

In order to explore this phenomenon further, an impulse test was conducted by pushing down on a magnet with a finger and releasing, in order to determine the resonant frequency of the torsional system. The resulting response to this impulsive input excitation can be seen in Fig. 28 in Appendix A. It was determined that the resonant frequency of the system was approximately 30 Hz. A reinforcement bracket was then placed on the load cell platform in an attempt to remove compliance in this component of the torque system, with the aim of shifting the resonance frequency. The reinforcement bracket is shown in Fig. 16.

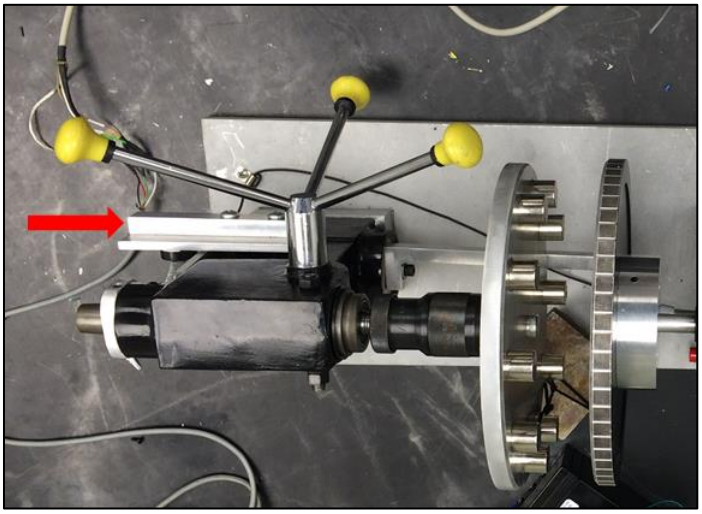

Figure 16: Reinforcement bracket placed on load cell platform

Preliminary measurements were conducted again and these oscillations in the torque were found to persist. Another impulse test was performed, the response of which can be seen in Fig. 19 in Appendix A , and the resonant frequency can be seen to have shifted slightly to 25 Hz. However, it was still close enough to the operation speed to excite oscillation in the torque measurement system.

In an attempt to dampen the excitation, a preload was placed on the torque system by hanging a weight on the magnets, as shown in Fig. 17.

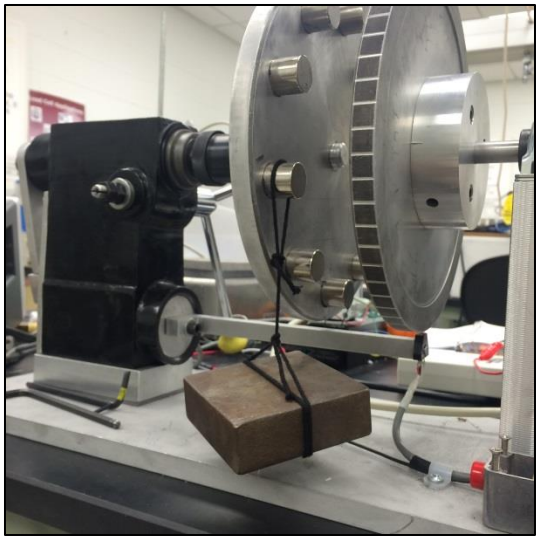

Figure 17: The 2.5 pound preload placed on torque system to dampen resonance

A new torque calibration curve was generated for this preload setup. This time, known weights were hung on the magnet disc in addition to the preload weight. The data points and calibration curve are shown in Table 7 and Fig. 30 in Appendix A. The preload was able to reduce the amplitude of oscillations by approximately 50 %, and an example of this improvement can be seen in Fig. 31 in Appendix A. Therefore, the preload setup and calibration was used to perform final measurements.

3.6 Measurement of Disk Temperature

An infrared (IR) pyrometer (OS152-MT IR Temperature Sensor, Omega) was used to measure temperature of the disk in a non-contact manner because the disk would be rotating at high speeds. The IR pyrometer pointed at the back face of the disk, with the sensor head approximately two inches away from the back face (the side not facing the magnets). It was pointed perpendicular to the face and approximately three inches radially outward from the center of the disk. To calibrate the pyrometer, the rotating disk was removed from the dynamometer and heated with a hot plate. The pyrometer was mounted two inches above the

disk and aimed perpendicular to the face at approximately three inches radially outward from the center. A thermocouple was placed on the disk approximately three inches radially outward from the center of the disk, as shown in Fig. 32 in Appendix A. Temperature from the thermocouple was recorded every 10 ^{o}F simultaneously with the pyrometer voltage output. The calibration data points and curve are given in Table 8 and Fig. 33 in Appendix A.

Chapter 4: Results and Discussion

4.1 Power Dissipation and Torque in the Simple and Schieber Models

Angular velocity, torque, magnetic field strength, and disk temperature were recorded at eight different magnet distances. Five trials, 60 seconds each, were performed at each distance. The original data from these trails can be found in Appendix A under Fig. 34. However, at the farthest distance the torque reading was so small that it could not be discerned from zero. Thus, only the results of the closer seven distances were analyzed. The trials at shim level one and two were only 10 seconds long in order to avoid damage to the motor at the lower speeds.

The angular velocity, torque, and magnetic field strength measurements were used to compare measured power dissipation (heat) of the benchtop model versus the predicted power dissipation from the Simple and Schieber theoretical models. Power dissipation was then determined by the product of measured torque and angular velocity. Predicted power dissipation was determined by inserting the measured angular velocity and measured magnetic field strength into the theoretical torque formulas and then the torque value was multiplied by the measured angular velocity. Disk and magnet geometry and conductivity values were also inserted into the

theoretical torque formulas. The disk and magnet geometry and conductivity values are given in Table 2.

Table 2: Disk geometry and materials property values for the Simple model and Schieber model

Property	Symbol	Value
Disk Radius	a	0.110 (m)
Center of Disk To Center of Magnet	R	0.089 (m)
Disk Thickness	t	0.012 (m)
Diameter of Magnet	D	0.019 (m)
Number of Magnets	N	10
Disk Conductivity	σ	2.66×10^7 (Siemens/m)

The torque in the Simple and Schieber models were multiplied by 10 – the number of magnets – in order to account for the fact that each magnet exerts a torque on the disk and these formulas only considered one magnet. Measured power dissipation and the predicted power dissipation from the Simple and Schieber models are shown in Fig. 18. The large gap without measurement points from about 50 rad/s (~500 rpm) to about 150 rad/s (~1,500 rpm) is due to the motor's torque-speed characteristics. At a point when applied load (i.e resistive torque) exceeds the motor's capabilities, the motor's speed quickly decreases to speeds that are a fraction of the intended operating speeds.

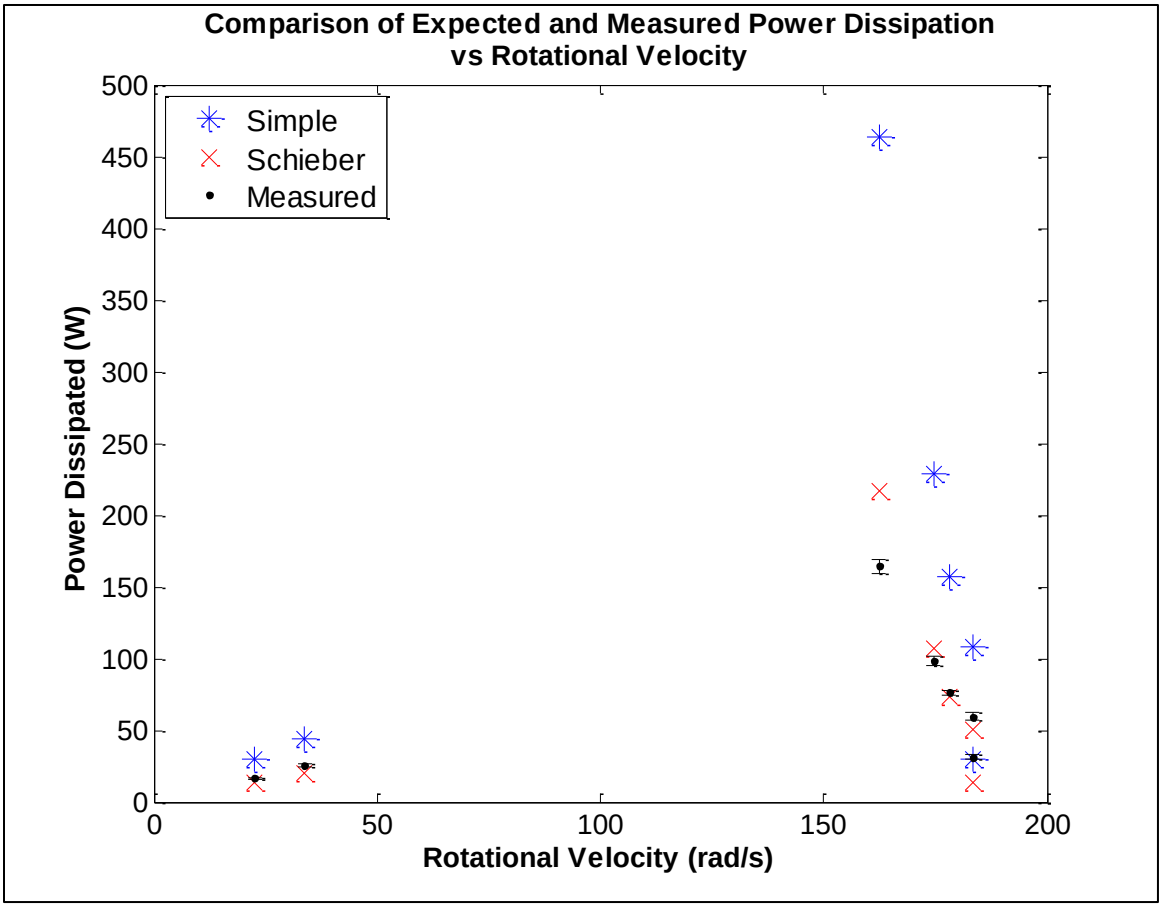

Figure 18: Comparison of the measured power dissipation to the predicted power dissipation from the Simple model and Schieber model

From Fig. 18 it can be seen that the Simple model greatly overestimates the power dissipation at values higher than 50 Watts. At the highest power dissipation level, 164 Watts, the Simple model is nearly triple at 464 Watts. An explanation for this deviation is provided in the next section, which discusses torque. Therefore, the Simple model is not an accurate model to predict the power dissipation of an ECWH. The Schieber model, however, did a more impressive job predicting the power dissipation. Predictions of the Schieber model were within 21% of the measured values for all but two distances. A comparison of the Schieber model and measured values are given in Table 3. It can be seen from Table 3 that the Schieber model overestimates power dissipation by 32% at the highest power dissipation level.

Table 3: Comparison of measured power dissipation versus Schieber model's predicted power dissipation

Shim Number	Angluar Velocity (rad/s)	Schieber Model Power Dissipation (W)	Measured Power Dissipation (W)	Difference (%)
1	23	13.88	16.1	-14%
2	34	20.39	25.85	-21%
3	162	217.37	164.26	32%
4	175	107.22	98.46	9%
5	178	73.62	76.55	-4%
6	183	50.89	59.74	-15%
7	183	16.96	31.34	-46%

The torque values predicted by the theoretical models are also compared to the measured values, as can be seen in Fig. 19. The black line is a reference line showing where the measured torque would be on the y-axis.

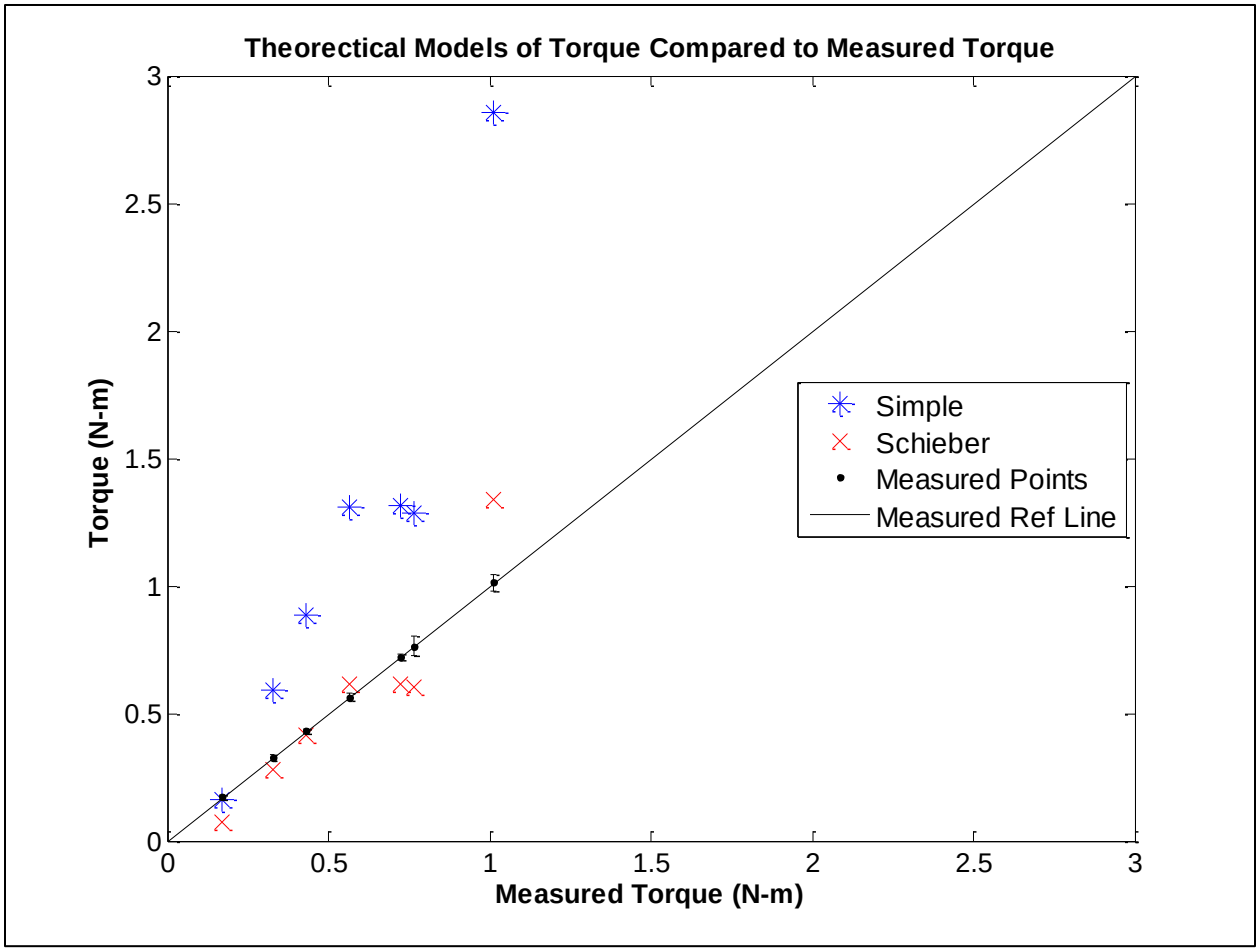

Figure 19: Comparison of measured torque to predicted torque of the Simple model and Schieber model

Corresponding to power dissipation, the expected torque from the Simple model greatly overestimates all values except at the operating condition corresponding to the lowest torque. This discrepancy is most likely due to the fact that the Simple model does not consider the current flow outside the area of the magnet. Consequently, there is less resistance in the disk and thus more current is induced, which then means higher torque and power dissipation.

The Schieber model is within 21% of the measured value for all torque readings except at those operating conditions where the torques are lowest and highest, where it is 44% and 32% off respectively. These larger errors are too high for the Schieber model to be used as a

predictive model for the torque design parameter. If it were not for these larger deviations, it would seem the Schieber model predicts the paths of the induced eddy currents throughout the disk quite well. Accurately knowing the paths of the eddy currents means the resistance from the disk is known which then translates to a more accurate prediction of the amount of current which then translates to sound torque and power predictions. The large deviations at low and high torques seem to illustrate the error in the Schieber model's underlying assumptions that the rotating disk has infinite conductivity and infinitesimally small thickness. Furthermore, the large deviations seem to indicate that the eddy currents might travel differently than predicted by the Schieber model under present experimental conditions. The Schieber model underestimates the torque at operating conditions corresponding to low values of torque. It is possible that the eddy currents do not travel as far outward from the magnet area when it is under low torque. In contrast, the Schieber model overestimates the torque at operating conditions corresponding to high torque values.

It can also be seen in Fig. 19 that the models increasingly over-predict the torque as the measured torque values increase except at around the 0.7 N-m mark. The two values here plateau, which were at low angular speeds. Thus, angular speed might affect eddy current paths as well, which the models do not consider. The skin effect could possibly have a profound effect on the eddy current paths. The skin effect is the tendency of current to concentrate at the surface of a conductor when the conductor experiences changes in electromagnetic fields at high frequencies. The skin depth is given by [17]:

$$\boldsymbol{\delta = \frac{1}{\sqrt{\pi f \mu \sigma}}} \qquad \textbf{(7)}$$

where, δ is the skin depth, f is the frequency of the electromagnetic field, μ is the magnetic permeability of the material experiencing the electromagnetic field, and σ is the conductivity of the material experiencing the electromagnetic field. It is likely that the induced eddy currents in the disk are concentrating at the surface of the disk and not traveling through its entire thickness, which the models do not consider. δ designates the depth at which the current density is 37% of the current density at the surface of the material [17]. Thus, it designates the depth at which the majority of currents are induced. In the present experiments, the frequency of the changing electromagnetic field is based on the disk's rotational velocity because the change in applied magnetic field arises from the discrete arrangement of the magnets. It is known that,

$$\boldsymbol{f = \frac{\omega}{2\pi}}$$

However, the frequency of the change in magnetic field in an ECWH is not given by this expression. This equation assumes there is only one change in the magnetic field for every complete rotation of the disk. However, every time the disk rotates past a magnet it experiences two changes in magnetic field: entering and exiting the magnetic field. Thus, the expression needs to be multiplied by a factor of two per magnet. Furthermore, the number of magnets is inserted into the expression because the rate at which the disk experiences a magnet is affected by how many magnets there are. In the case of the configuration of the present experiment, for every complete rotation, the disk experiences 10 magnets. The frequency of the magnetic field in the case of this experiment, then, is given by,

$$\boldsymbol{f = \frac{\omega}{2\pi} * 2 * N = \frac{\omega}{2\pi} * 2 * 10 = \frac{10\omega}{\pi}} \qquad \textbf{(8)}$$

Therefore, the skin depth for the experimental configuration in this work is,

$$\delta = \frac{1}{\sqrt{10\omega\mu\sigma}} \quad \textbf{(9)}$$

Since the skin effect may possibly explain the discrepancy between model predictions and measurements, its effect on the torque and power dissipation is examined next.

4.2 Power Dissipation and Torque Considering Skin Effect

The skin effect may be incorporated relatively easily in the Simple and Schieber models by replacing the thickness of the disk with the skin depth at angular speeds where the skin depth is smaller than the disk thickness. Fig.20 shows the expected power dissipation from the Simple and Schieber models considering the skin effect using this approach.

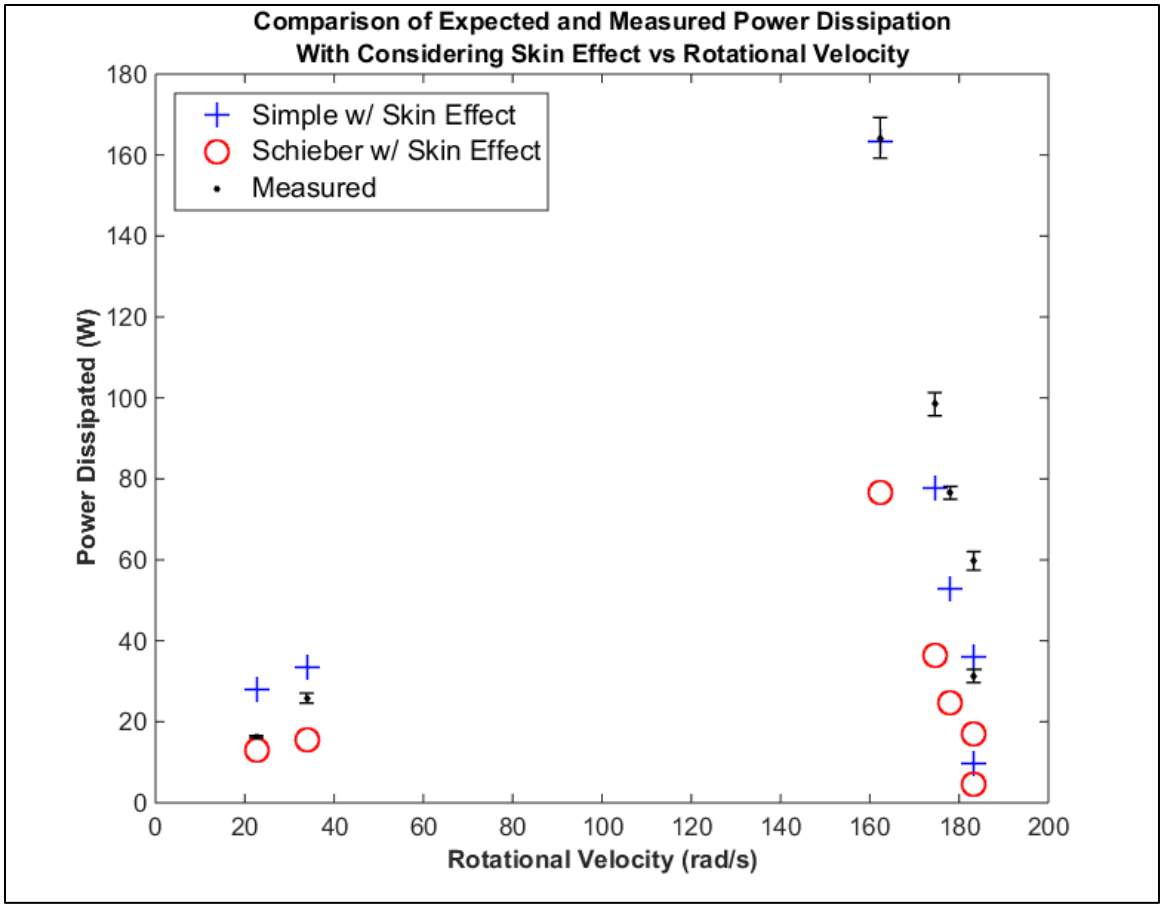

Figure 20: Comparison of measured and expected power dissipation with Simple model and Schieber model considering skin effect

It can be seen from Fig. 20 that the expected power dissipation at the two lower rotational speeds is nearly the same as the earlier predictions based on the disk thickness because the speeds are too low for the skin effect to be impactful. At these low speeds (hence low frequencies) the skin depth is barely less than the thickness of the disk therefore the current still travels through nearly the entire thickness of the disk. At the higher speeds (hence higher frequencies) the skin effect makes a significant impact on predicted values. The Simple model predicts power dissipation closer to the measured values compared to not including the skin effect, while the Schieber model now greatly underpredicts the measured values. The Simple model predicts the power dissipated within one percent of the measured value at the highest power dissipation value: 164

W. Without considering skin effect the Simple model overpredicted the 164 W value by a factor of 3. The Simple model underpredicts measured values as the angular velocity increases, indicating that inclusion of the skin effect might be exaggerated or that its effects are not fully captured by simply substituting δ for the disk thickness in Equation 9.

Torque predictions considering the skin effect are compared to measured values as well and are shown in Fig. 21.

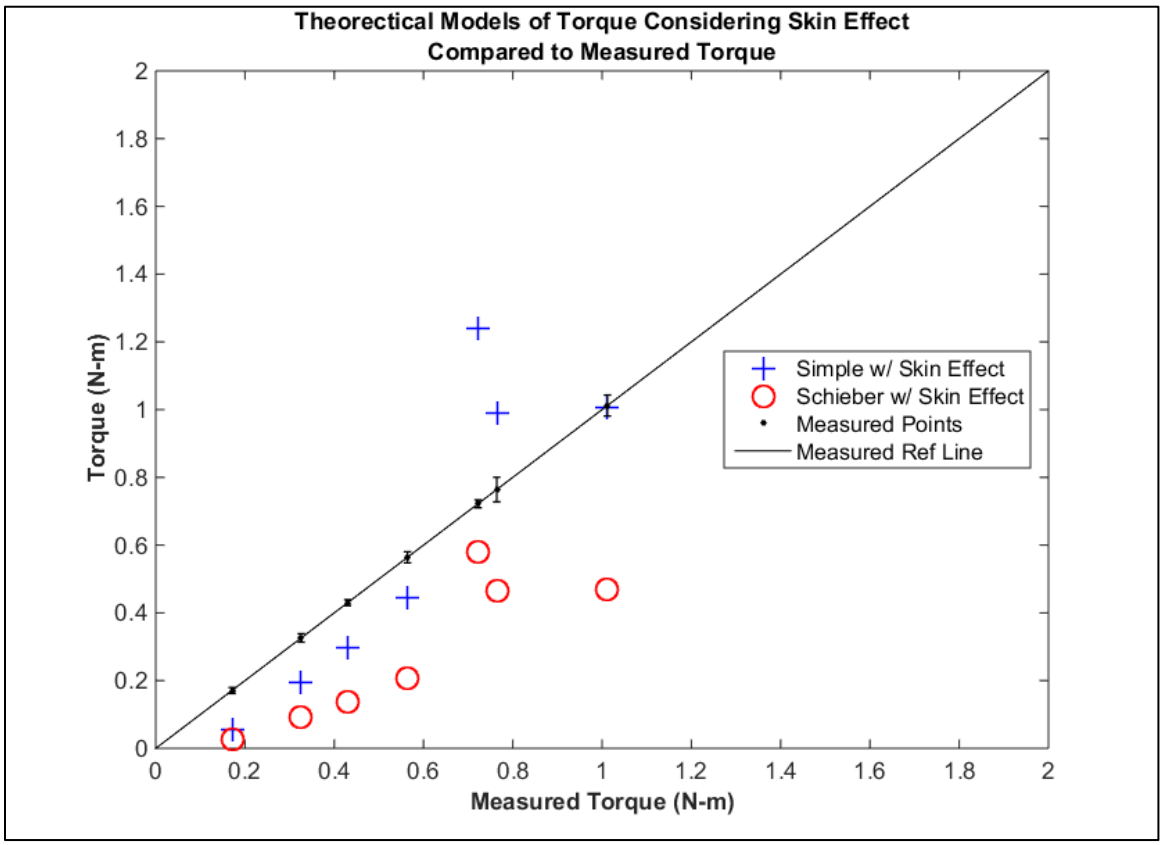

Figure 21: Comparison of measured and expected torque with Simple model and Schieber model considering skin effect

The Schieber model including the skin effect greatly underpredicts the measured torque. The Simple model with the skin effect shows better agreement with measurements than the Schieber model including the skin effect and compared to the Simple model not including the skin effect.

However, at the measured torque value of approximately 0.2 N-m, corresponding to the point of highest speed, the Simple model with skin effect underpredicts by a factor of three. Additionally, at the measured torque value of approximately 0.7 N-m, corresponding to the point of lowest speed, the Simple model with the skin effect overpredicts measurements by more than 40 %. These large fluctuations make the Simple model with skin effect unable to be considered an accurate predictive model. Comparisons of measurements with the Schieber model with skin effect show that this model cannot be applied to scenarios with a large number of magnets and operation involving high angular speeds either. The eddy current paths under these conditions must be considerably different than those predicted by the Schieber model. This comparison underscores the need for development of a better predictive theory for ECWH.

4.3 Measurement of Temperature Rise due to Eddy Currents

In addition to torque and power dissipation measurements, temperature rise in the disk over 10 minutes was recorded at five distances (Shim 3 to Shim 7). Distances (i.e. magnetic field strengths) corresponding to Shim 1 and 2 were not tested as the motor speeds at these distances were too low to run the motor for a prolonged period without possibly incurring damage. The temperature rise of the disk over 10 minutes at the highest power dissipation level, 164 Watts, corresponding to the third closest magnet distance, Shim 3, is shown in Fig. 22. The Shim 3 distance is 0.493 inches, corresponding to 0.493 T.

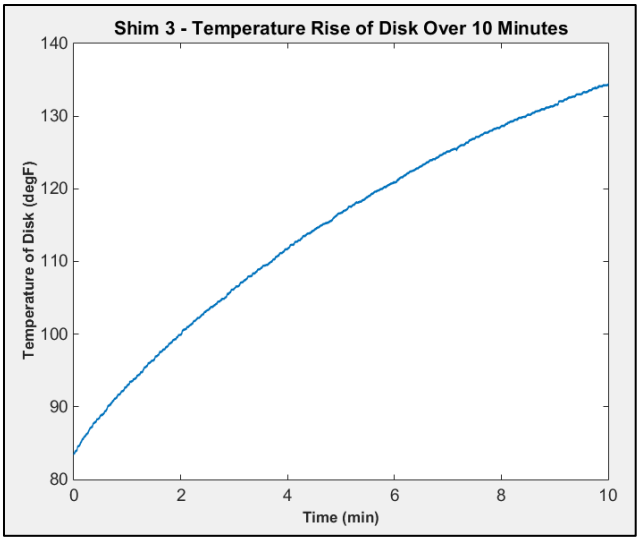

Figure 22: Temperature rise of the disk at highest power dissipation level

At the Shim 3 distance the 2.5 pound aluminum disk rose by 50 ^{o}F in just 10 minutes, demonstrating the heating power of the eddy currents. Temperature was measured on the back of the disk, approximately three inches radially outward from the center of the disk. The center of the magnet poles are approximately 3.5 inches away from the center of the disk. It is reasonable to assume this temperature measurement location is representative of the entire disk temperature because aluminum has a high thermal conductivity. Furthermore, after this trial, the disk was felt to be scalding hot (greater than 115 ^{o}F) over the entire disk. The disk was spinning at 162 rad/s (1,550 rpm) under these conditions of maximum heating. In comparison, at the Shim 6 distance (0.752 inches, 0.214 T) the temperature rises only 20 ^{o}F even though the disk is spinning at a faster angular speed of 183 rad/s (1,750 rpm). This highlights the need for development of more accurate theoretical models as the interaction between magnetic field strength, angular velocity, torque, and heat are coupled and difficult to de-convolve. One of these variables cannot be independently changed without affecting the others. These temperature measurements prove that an ECWH can indeed supply significant heating but that optimization

is needed, which in turn depends on accurate design parameters, reinforcing the need for better understanding the torque design parameter via accurate, physically correct modeling.

4.4 Dimensional Analysis

In addition to the measurements from the benchtop experimental model, dimensional analysis was performed to find key dimensionless parameters relevant to ECWH and to infer corresponding relationships of critical parameters necessary for design of a prototype. The list of variables considered are listed in Table 4, where the repeated variables are highlighted.

Table 4: Variables considered for dimensional analysis

Symbol	Variable
Q	Heat Generation
B	**Magnetic Field Strength**
l	Distance from Magnet
t	Thickness of Disk
a	**Radius of Disk**
σ	Electrical Conductivity of Disk
ω	**Angular Velocity of Disk**
ρ	**Density of Disk Material**
T	Torque
Cp	Specific Heat Capacity of Disk
K	Thermal Conductivity
μ_o	Magnetic Permeability of Disk
Temp	**Temperature of Disk**

Using the Buckingham Pi Theorem, the resulting dimensionless groups are identified and are listed in Table 5.

Table 5: List of dimensionless terms

$\pi_1 = \frac{jB}{a\rho\omega^2}$
$\pi_2 = \frac{\sigma B^2}{\omega\rho}$
$\pi_3 = \frac{T}{\omega^2\rho a^5}$
$\pi_4 = \frac{C_p Temp}{\omega^2 a^2}$
$\pi_5 = \frac{K\,Temp}{a^4\rho\omega^3}$
$\pi_6 = \frac{\mu_o a^2\omega^2\rho}{B^2}$
$\pi_7 = \frac{l}{a}$
$\pi_8 = \frac{t}{a}$

It is found that the ratio $\Pi_A=\Pi_2/\Pi_3$, results in a physically significant dimensionless group for the experimental results presented here:

$$\frac{\boldsymbol{\Pi_2}}{\boldsymbol{\Pi_3}} = \boldsymbol{\Pi_A} = \frac{\boldsymbol{\sigma B^2\omega^2 a^5}}{\boldsymbol{T\omega}} \qquad \textbf{(10)}$$

The numerator is representative of the heat generated by eddy currents. It can be seen that Equation 10 is similar to Equations 3 and 6. The denominator represents the input power from the motor. Thus Π_A is a ratio of heat generated by dissipation of eddy currents and input power. For the experimental conditions considered in this thesis, Π_A values at the seven shim distances ranged from 19 to 57. Π_A follows the same trend versus angular velocity as the characteristics of

the motor (power dissipated vs. angular velocity curve), as shown in Fig. 23, indicating that Π_A is a good representation of power dissipated by the experimental model.

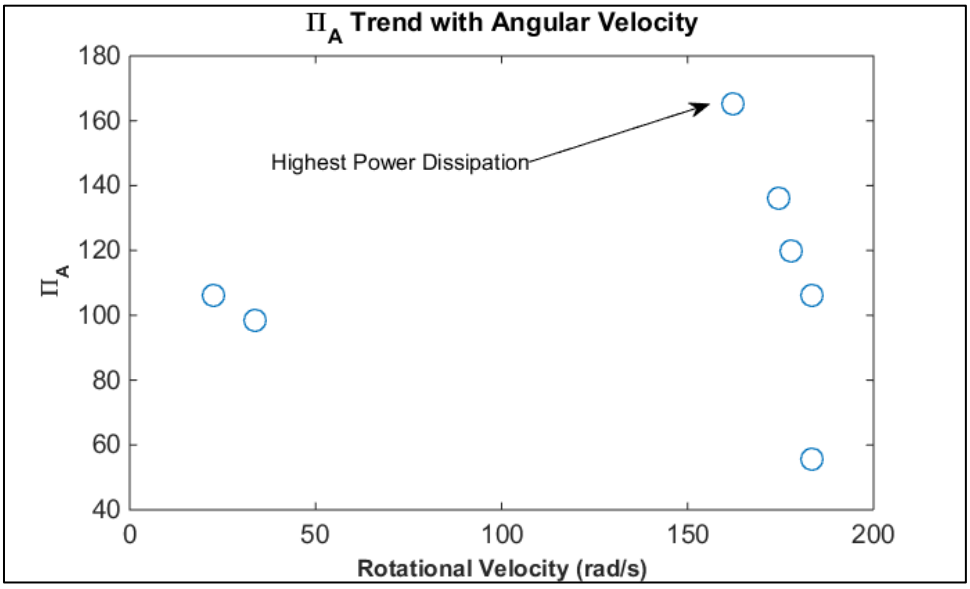

Figure 23: Π_A's trend with angular velocity, illustrating similarity to the motor power-speed curve

This dimensionless term allows for scaling up to a residential scale prototype as it incorporates the most crucial variables. Relationships between dimensionless terms were explored to determine if informative relationships existed that could help provide design parameters. An interesting relationship was found between Π_A and Π_4, as can be seen in Fig. 24.

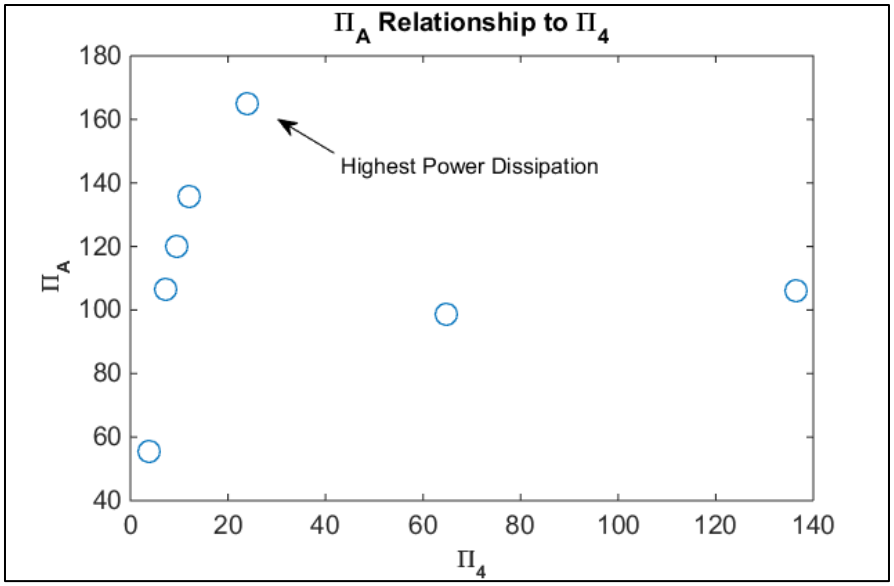

Figure 24: The relationship between Π_A and Π_4

There appears to be an opportunity for optimizing Π_A with respect to Π_4, possibly between Π_4 values of 20 and 40. This is informative because higher values of Π_A correlate to the higher values of power dissipation. Thus, it is known what values of Π_4 the design parameters need to fall within to optimize the heating capabilities of a prototype. Additionally, Π_4 contains specific heat capacity and temperature rise of the disk, design parameters that Π_A does not contain.

Interesting relationships are also found between Π_4 and Π_2 and Π_3. A plot showing the effects of the inverse of Π_2 on Π_4 is shown in Fig. 25.

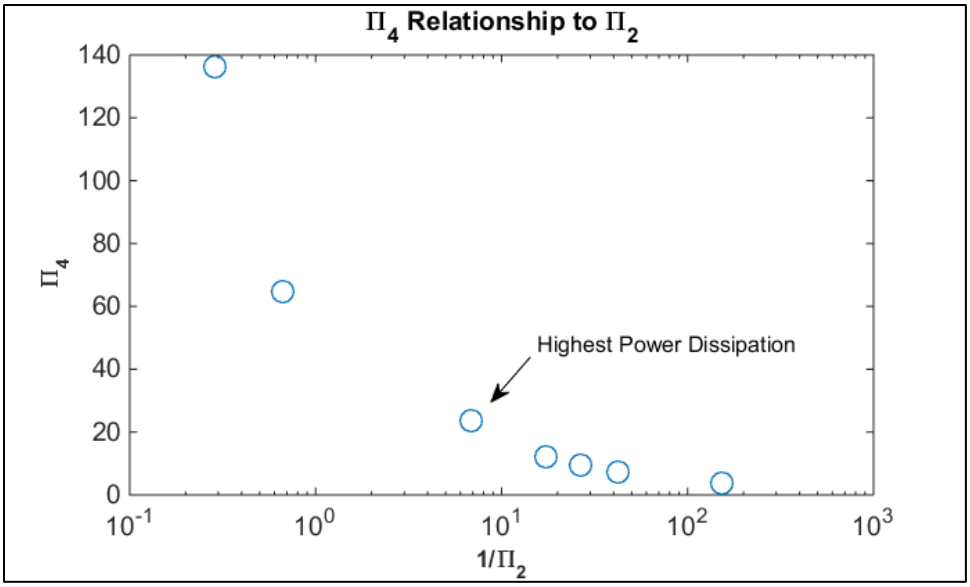

Figure 25: The relationship between Π_4 and 1/ Π_2

Again, there appears to be an optimization range with respect to values of the non-dimensional terms. Here, a range between 4 and 10 for $1/\Pi_2$ is optimal. Relating Π_4 to Π_2 is helpful because it allows designs to be made without needing to assume a torque value, which is needed when Π_4 is related to Π_A. Lastly, Π_4 also has an informative relationship with Π_2 as shown in Fig. 26.

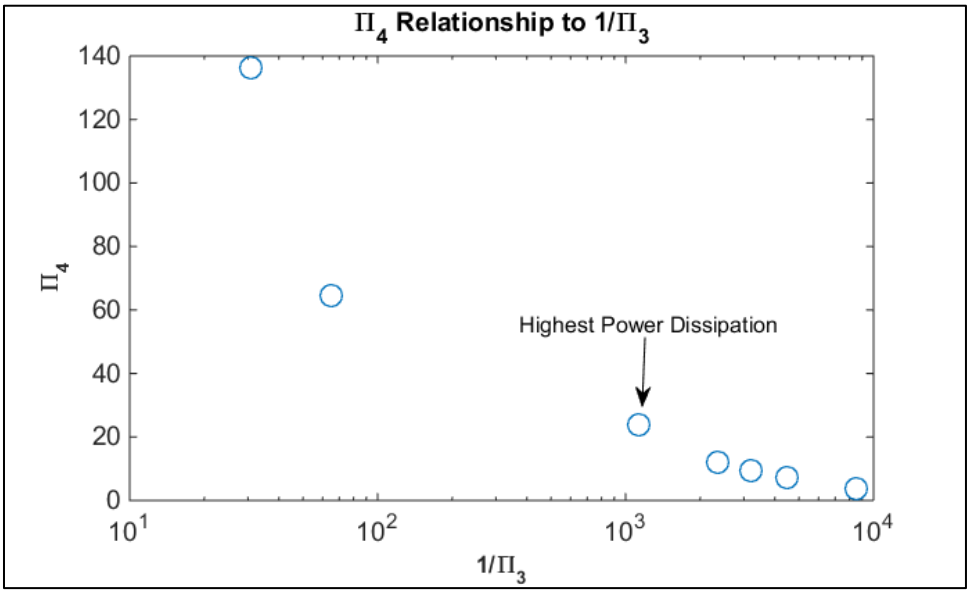

Figure 26: The relationship between Π_4 and 1/ Π_3

Here, the highest power dissipation is in a range between 700 and 2,000 for $1/\Pi_3$, which is instructive since Π_3 includes a different combination of design parameters than the other previously mentioned non-dimensional pi groups.

Being able to constrain designs between ranges of non-dimensional parameters will greatly help when determining design parameters for a prototype with similar geometries, kinematics, and dynamics to the benchtop model. As an illustrative example of how the foregoing dimensional analysis and the experimental results presented here may be used for designing a residential scale ECWH prototype is described next.

Consider a reasonable sized rotating, heating disk that would fit in a home hot water storage tank – one foot in diameter or 0.30 meters and one inch thick or 0.0254 meters. In order to use cheaper material for the heating disk, aluminum 6061 is selected. Next, the necessary heating capabilities must be identified. The typical home in the United States consumes 3,000 kWh of energy per year for hot water heating, which is equivalent to requiring approximately 340 W of constant power [18]. Then, assuming the heat transfer from the heating disk of the ECWH to the water is not perfect, it is determined the heat generated in the ECWH heating disk needs to be 1.5 times that of the heat needed to be supplied to the water since heat transfer coefficients can be off by as much as 50%. In this case, the ECWH heating disk needs to generate 510 W of heat. Heat generated can be determined by temperature rise of the disk using:

$$Q = mc_p\Delta T$$

Since the required heat generation is known, the necessary temperature rise can be determined:

$$\Delta T = \frac{Q}{mc_p} = \frac{510\ W}{(5.00\ kg) * (896 \frac{J}{kg℃})} = 0.11\ \frac{℃}{s}$$

Now, the dimensionless terms can be utilized to select an appropriate sized wind turbine. Π_4 contains temperature rise as a variable. From the present experimental results it is known that Π_4 should be between 20 and 40 for optimal heating. This can then be used to determine the necessary angular velocity of the wind turbine, assuming a value of Π_4=30.

$$\Pi_4 = \frac{c_p \Delta T}{\omega^2 a^2}$$

$$\omega = \sqrt{\frac{c_p \Delta T}{\Pi_4 a^2}} = \sqrt{\frac{(896 \frac{J}{kg℃})(0.11\ \frac{℃}{s} * 60\ s)}{(30) * \left(\frac{0.3\ m}{2}\right)^2}} = 93.6\ rad/s$$

Note the temperature rise per second was multiplied by 60 seconds because that is how long the duration of the experimental runs were in this work which defined the dimensionless term values. Now with a known desired angular velocity, a vertical axis wind turbine can be selected that operates at maximum output near the specific angular velocity for a common wind speed. Suppose a wind turbine is selected that has a torque of 6 N-m at 93.6 rad/s. Now, the necessary magnetic field strength needed to apply the resistive torque of 6 N-m can be determined using Π_A:

$$\Pi_A = \frac{\sigma B^2 \omega^2 a^5}{T\omega}$$

It is known, from the benchtop model that optimum heating occurs at values of Π_A near 160. Thus, the required magnetic field strength can be calculated to be,

$$B = \sqrt{\frac{\Pi_A T \omega}{\sigma \omega^2 a^5}} = \sqrt{\frac{(160)(6\ N-m)(93.6\frac{rad}{s})}{\left(2.667*10^7\frac{Seimens}{m}\right)\left(93.6\frac{rad}{s}\right)^2\left(\frac{0.3}{2}\right)^5}} = 0.69\ \text{T}$$

Now, the number of magnets, strength of magnets, and the distance at which they are spaced from the disk can be determined to provide a cumulative 0.69 T magnetic field strength – an achievable amount with an array of 15 or more permanent magnets.

This illustrative example demonstrates how the dimensionless pi groups from the dimensional analysis can be used for designing a prototype. The foregoing example also highlights the feasibility of an ECWH as a practical device.

Chapter 5: Conclusions and Recommendations for Further Work

5.1 Summary and Conclusions

A benchtop experimental model apparatus has been used to experimentally investigate the physical relationships between key parameters for ECWH, namely angular velocity, magnetic field strength, resistive torque and disk and magnet geometries. The present study has focused on resistive torque as it is a major practical constraint for designing ECWHs that use wind or hydro turbines. Experimental measurements on magnetic field strength, angular velocity, torque, and temperature were performed on the benchtop model. The measured values of torque and dissipated power have been compared to four theoretical models: Simple model, Simple model with skin effect, Schieber's model, and Schieber's model with skin effect.

The Simple model grossly overpredicts the measured torque and dissipated power, confirming that the electrical resistance the flowing eddy current experiences outside the magnet area is significant. Schieber's model, which accounts for the resistance of the eddy current paths outside the magnet area, but also assumes the disk to have infinitely large conductivity and infinitesimally small thickness, appears to predict the measured resistive torque and dissipated power the best. However, the Schieber model does not prove to be reliable since it deviates 32% from measured values at the highest power value. Incorporating the skin effect into Schieber's model does not improve its predictability, which raises the question of whether or not the skin effect is exaggerated or whether Schieber's model is not applicable to designs with more than one magnet and with disks with considerable thickness. Incorporating the skin effect into the Simple model improved its predictions, but it still was not as accurate as Schieber's model. The experimental conditions examined in this thesis involve 10 magnets and operation at high speeds, which appear to greatly complicate predictions of resistive torque and heating due to more complex eddy current paths.

Dimensional analysis reveals a significant pi group that could be used to scale the model to a residential sized prototype if geometric, kinematic, and dynamic similarity are maintained. Furthermore, numerous relationships discovered between pi groups provide information to optimize a residential scale prototype design. Lastly, an illustrious example using the significant pi group and the optimization relationships between other pi groups shows the feasibility of a residential sized ECWH as all the design parameters were realistically achievable.

5.2 Recommendations for Further Work

A more focused study on eddy current paths is needed if accurate and predictive models can be developed and validated. Future studies should vary the number of magnets, their spacing, and their sizes in order to get a better understanding on how these geometries affect the accuracy of existing models and to develop a new theoretical model that captures the essence of the experimental results. Future studies should also consider varying the thickness of the rotating disk in order to investigate the skin effect.

References

[1] "U.S. Energy Information Administration - EIA - Independent Statistics and Analysis."Heating and cooling no longer majority of U.S. home energy use. 07 Mar. 2013. U.S. Energy Information Administration. 13 Feb. 2014 <http://www.eia.gov/todayinenergy/detail.cfm?id=10271&src=%E2%80%B9%20Consumption%20%20%20%20%20%20Residential%20Energy%20Consumption%20Survey%20%28RECS%29-b1>.

[2] "New Infographic and Projects to Keep Your Energy Bills Out of Hot Water." Energy.gov. 19 Apr. 2013. U.S Department of Energy. 5 Feb. 2014 <http://energy.gov/articles/new-infographic-and-projects-keep-your-energy-bills-out-hot-water>.

[3] "The Faraday Disk Dynamo as the Original Over-Unity Device." Faraday-Disk. 25 Mar. 2005. The Time Machine Project. 13 Feb. 2014 < http://u2.lege.net/cetinbal/faradaydisk.htm >.

[4] Montgomery, H. "Current Flow Patterns in a Faraday Disc." European Journal of Physics 25 (2004): 171-83.

[5] "Finding an Electromagnetic Analog for the Falaco Soliton." Turbomagnetics Research Associates. Turbomagnetics Research Associates. 13 Feb. 2014 <http://www.ussdiscovery.com/FalacoSolitonMagnetic001.htm>.

[6] "Windmills for Hot Water." The Back Shed. N.p., 19 July 2006. Web. 10 Sept. 2014. <http://www.thebackshed.com/forum/forum_posts.asp?TID=230>.

[7] Dirba, Kleperis. Practical Applications of Eddy Currents Generated by Wind". Proc. of Annual Conference on Functional Materials and Nanotechnologies. 2011. IOP Publishing.

[8] Liu, Xiaohung, Chuican Chen, Hongdong Yu, Guidan Wei, and Zhende Tian. The Study of the Heat Device in Wind-Magnetic Water Heater. Proc. of Advanced Materials Research. 2011. Trans Tech Publications.

[9] Richardson, Ed, Peter Dent, Aimee Shirk, and Jeff Green. The US Magnet Materials Story Past-Present-Future. Issue brief. US Magnet Materials Assoication. <http://www.electronenergy.com/media/USMMA%20Presentation%20General%2012-07.pdf>.

[10] Fireteanu, Virgiliu, and Onur Nebi. Finite Element Electromagnetic 2D Model of an Eddy Current Heater with Rotating Permanent Magnets. Proc. of Electrical Engineering Series, University of Craiova. 2008. Annals of the University of Craiova.

[11] Nebi, O., and V. Firetenau. Finite Element Analysis of an Eddy Current Heater for Wind or Water Kinetic Energy Conversion into Heat. Proc. of International Conference on Renewable Energies and Power Quality, Granada, Spain. 25 Mar. 2010. European Association for the Development of Renewable Energies.

[12] Tudorache, Tiberiu, and Mihail Popescu. FEM Optimal Design of Wind-Energy Based Heater. 2009. Acta Polytechnica Hungrica.

[13] Gosline, Campion, and Hayward. On The Use of Eddy Current Brakes as Tunable, Fast Turn-On Viscous Dampers for Haptic Rendering. Proc. Eurohaptics 2006, pp. 229-234, 2006.

[14] W. R. Smythe, “On eddy currents in a rotating disk”, Electrical Engineering, vol. 61, pp. 681-684, 1942.

[15] D. Schieber, “Braking torque on rotating sheet in stationary magnetic field”, Electrical Engineers, Proceedings of the Institution of, vol. 121, pp. 117-122, 1974.

[16] J. H. Wouterse, “Critical torque and speed of eddy current brake with widely separated soft iron poles”, Electrical Power Applications, IEE Proceedings B, vol. 138, pp. 153-158, 1991.

[17] "Depth of Penetration & Current Density." *NDT Education Research Center*. N.p., 2014. Web. <https://www.nde-ed.org/EducationResources/CommunityCollege/EddyCurrents/Physics/depthcurrentdensity.htm>.

[18] "Energy Use in Homes." U.S Energy Information Administration, 5 Feb. 2013. Web. 15 Apr. 2015. <http://www.eia.gov/energyexplained/index.cfm?page=us_energy_homes>.

Appendix A

Supplementary Figures and Tables

Table 6: Data points of load cell for torque calibration

LC Reading (V)	Actual Torque (ft-lbs)
0.523	0
0.544	0.129
0.599	0.37

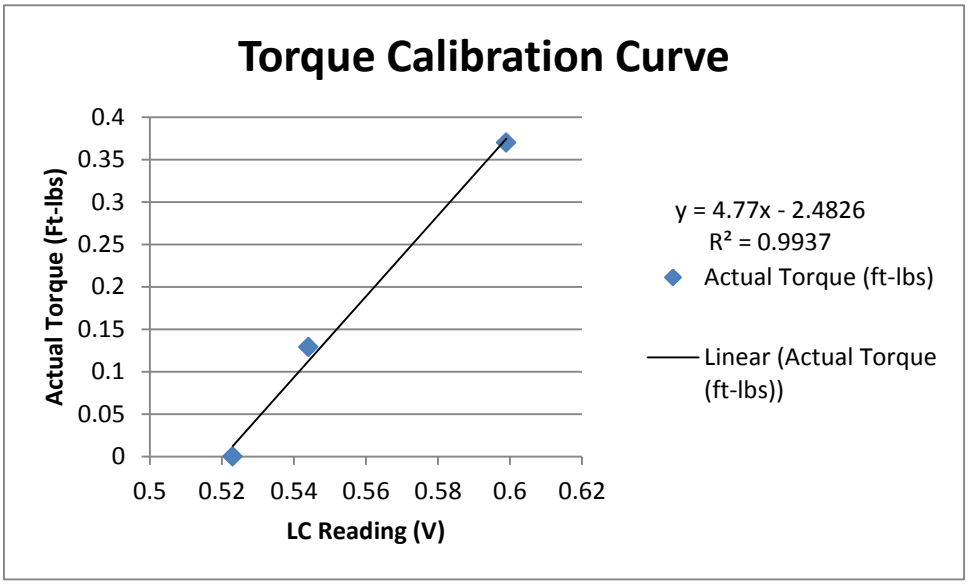

Figure 27: Torque calibration curve for load cell

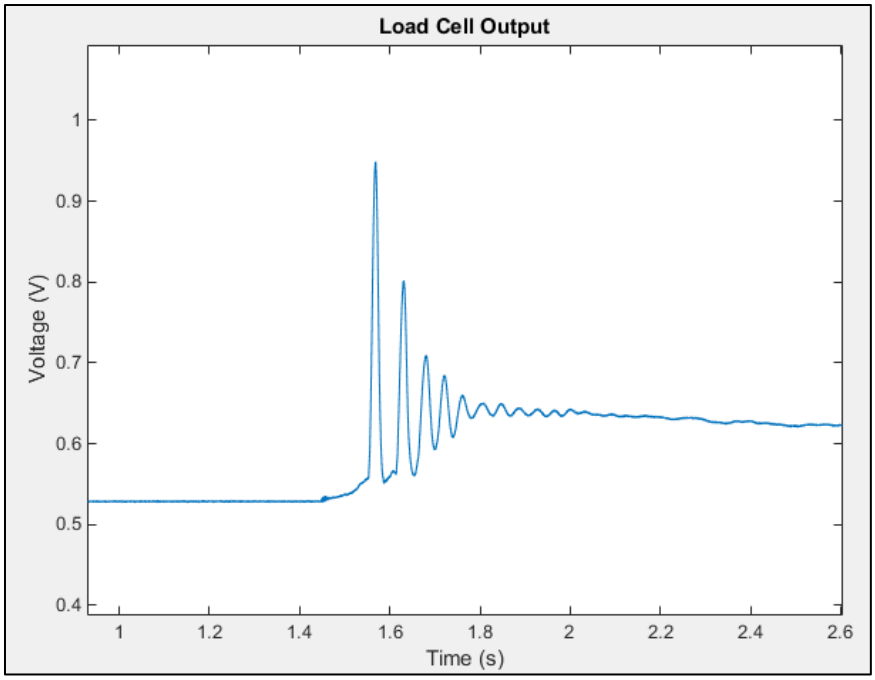

Figure 28: Impulse test on torque system to investigate resonance (frequency = 30 Hz)

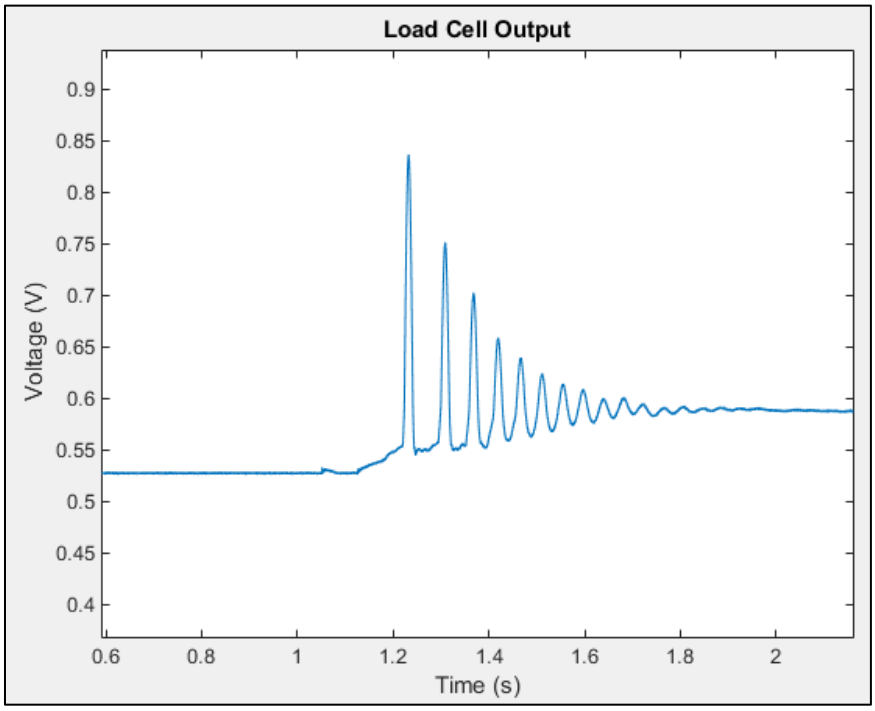

Figure 29: Impulse test with reinforced load cell bracket (frequency = 25 Hz)

Table 7: Data points for preload torque calibration curve

Weight (lbs)	LC Reading (V)	Diff in LC (V)	Diff in Torque (ft-lbs)	Actual Torque (ft-lbs)
0	0.523			0
2.538	0.679	0	0	0.742
2.979	0.707	0.028	0.129	0.871
3.798	0.758	0.079	0.369	1.111

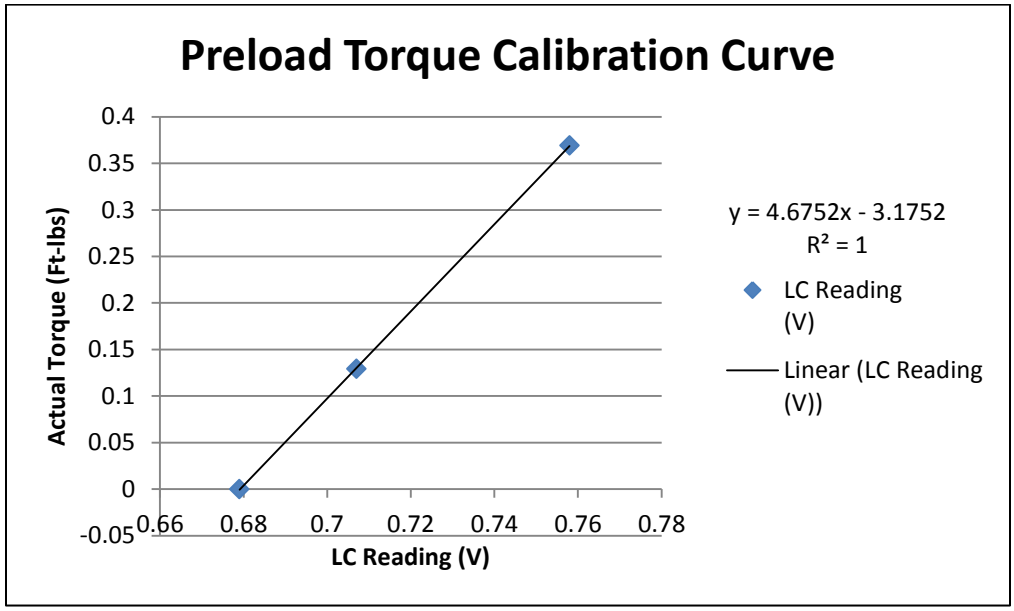

Figure 30: Torque calibration curve for preload setup

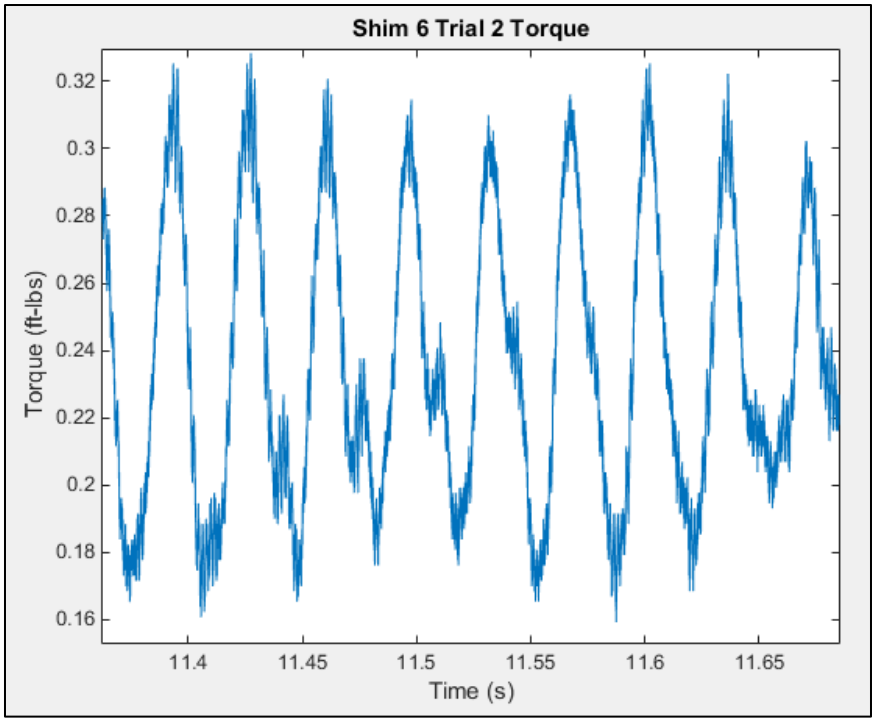

Figure 31: An example of decreased torque oscillation amplitude with preload

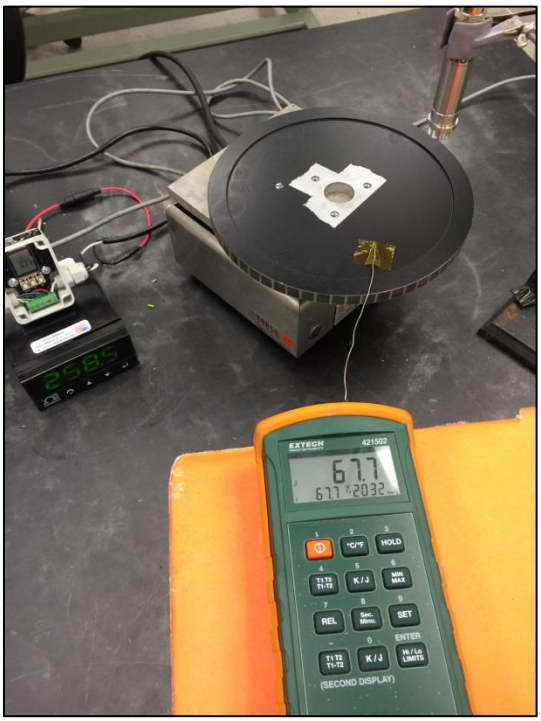

Figure 32: The setup of a thermocouple and heating plate used to calibrate the IR temperature sensor

Table 8: Calibration data points for the infrared temperature sensor

DAQ Voltage Reading (V)	Thermocouple Reading (°F)
2.523	67.8
2.7181	76.9
2.8707	85.3
3.063	94.9
3.256	105.3
3.451	115.1
3.637	125.2
3.838	134.5

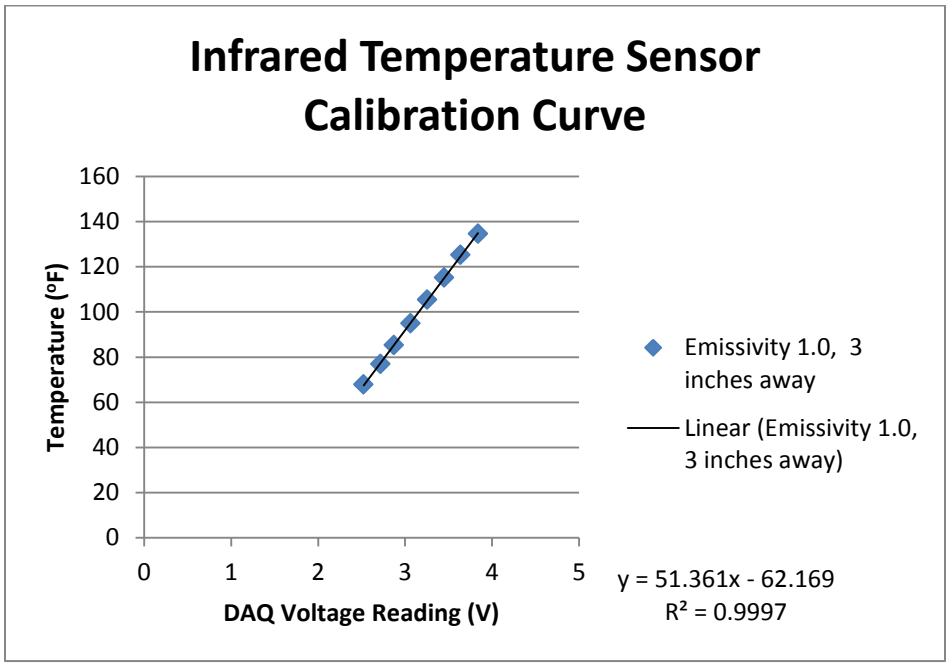

Figure 33: Calibration curve for the infrared temperature sensor

Shim #	Trial	Length of Time (sec)	Average Torque (ft-lb)	Angular Velocity (rpm)	Input Power (hp)	Temperature Change (degF)	Magnet Distance (in)	Magnetic Field Strength (T)	Date
8	1	60	0.0632	1750	0.021	0.26	1.216	0.089	1-Mar
8	2	60	0.053	1750	0.018	0.96	1.216	0.089	2-Mar
8	3	60	0.0661	1750	0.022	0.61	1.216	0.089	2-Mar
8	4	60	0.0593	1750	0.020	0.4472	1.216	0.089	2-Mar
8	5	60	0.0616	1750	0.021	0.5492	1.216	0.089	2-Mar
Average		**60**	**0.06064**	**1750**	**0.020**	**0.56528**	**1.216**	**0.089**	
7	1	60	0.136	1750	0.045	1.6	0.947	0.072	1-Mar
7	2	60	0.122	1750	0.041	2.1693	0.947	0.072	2-Mar
7	3	60	0.1298	1750	0.043	1.9668	0.947	0.072	2-Mar
7	4	60	0.121	1750	0.040	1.2247	0.947	0.072	2-Mar
7	5	60	0.122	1750	0.041	1.4578	0.947	0.072	2-Mar
Average		**60**	**0.126**	**1750**	**0.042**	**1.684**	**0.947**	**0.072**	
6	1	60	0.2352	1750	0.078	3.3354	0.752	0.049	2-Mar
6	2	60	0.2358	1750	0.079	3.601	0.752	0.049	2-Mar
6	3	60	0.2309	1750	0.077	3.2355	0.752	0.049	2-Mar
6	4	60	0.25	1750	0.083	3.3262	0.752	0.049	2-Mar
6	5	60	0.251	1750	0.084	3.0059	0.752	0.049	2-Mar
Average		**60**	**0.241**	**1750**	**0.080**	**3.301**	**0.752**	**0.049**	
5	1	60	0.3061	1700	0.099	4.0125	0.689	0.0318	2-Mar
5	2	60	0.3173	1700	0.103	4.7065	0.689	0.0318	2-Mar
5	3	60	0.3192	1700	0.103	4.2818	0.689	0.0318	2-Mar
5	4	60	0.3213	1700	0.104	3.9646	0.689	0.0318	2-Mar
5	5	60	0.3226	1700	0.104	3.5725	0.689	0.0318	2-Mar
Average		**60**	**0.317**	**1700**	**0.103**	**4.108**	**0.689**	**0.0318**	
4	1	60	0.3941	1667	0.125	5.1604	0.629	0.026	2-Mar
4	2	60	0.4196	1667	0.133	5.696	0.629	0.026	2-Mar
4	3	60	0.4209	1667	0.134	4.8036	0.629	0.026	2-Mar
4	4	60	0.4214	1667	0.134	4.6922	0.629	0.026	2-Mar
4	5	60	0.4224	1667	0.134	4.3437	0.629	0.026	2-Mar
Average		**60**	**0.416**	**1667**	**0.132**	**4.939**	**0.629**	**0.026**	
3	1	60	0.7058	1500	0.202	8.4984	0.493	0.021	2-Mar
3	2	60	0.7562	1562.5	0.225	9.5409	0.493	0.021	3-Mar
3	3	60	0.7559	1562.5	0.225	8.7134	0.493	0.021	3-Mar
3	4	60	0.7571	1562.5	0.225	8.2362	0.493	0.021	3-Mar
3	5	60	0.7581	1562.5	0.226	7.4139	0.493	0.021	3-Mar
Average		**60**	**0.747**	**1550**	**0.220**	**8.481**	**0.493**	**0.021**	
2	1	60	0.5159	307.5	0.030	1.0043	0.375	0.011	2-Mar
2	2	10	0.5739	325	0.036	N/A	0.375	0.011	2-Mar
2	3	10	0.5771	333	0.037	N/A	0.375	0.011	2-Mar
2	4	10	0.5774	325	0.036	N/A	0.375	0.011	2-Mar
2	5	10	0.5742	325	0.036	N/A	0.375	0.011	2-Mar
Average		**60**	**0.564**	**323.1**	**0.035**		**0.375**	**0.011**	
1	1	60	0.5115	220	0.021	0.9422	0.311	0.0048	2-Mar
1	2	10	0.5323	218.75	0.022	N/A	0.311	0.0048	2-Mar
1	3	10	0.5329	214.3	0.022	N/A	0.311	0.0048	2-Mar
1	4	10	0.5336	216.7	0.022	N/A	0.311	0.0048	2-Mar
1	5	10	0.5323	214.3	0.022	N/A	0.311	0.0048	2-Mar
1	6	10	0.5301	214.3	0.022	N/A	0.311	0.0048	2-Mar
Average		**60**	**0.532**	**215.67**	**0.022**		**0.311**	**0.0048**	

Figure 34: Original data from the 60 second trials